DENSITY MEASUREMENTS OF NEUTRAL XENON USING MULTIPHOTON IONIZATION AND MICROWAVE SPECTROSCOPY IN A HALL EFFECT THRUSTER

THESIS

Taylor J. Foy

AFIT-ENY-MS-21-M-329

DEPARTMENT OF THE AIR FORCE
AIR UNIVERSITY

AIR FORCE INSTITUTE OF TECHNOLOGY

Wright-Patterson Air Force Base, Ohio

DISTRIBUTION STATEMENT A.
APPROVED FOR PUBLIC RELEASE; DISTRIBUTION UNLIMITED.

AFIT-ENY-MS-21-M-329

DENSITY MEASUREMENTS OF NEUTRAL XENON USING MULTIPHOTON IONIZATION AND MICROWAVE SPECTROSCOPY IN A HALL EFFECT THRUSTER

THESIS

Presented to the Faculty

Department of Aeronautics and Astronautics

Graduate School of Engineering and Management

Air Force Institute of Technology

Air University

Air Education and Training Command

In Partial Fulfillment of the Requirements for the

Degree of Master of Science in Astronautical Engineering

Taylor J. Foy, BS

March 2021

DISTRIBUTION STATEMENT A.
APPROVED FOR PUBLIC RELEASE; DISTRIBUTION UNLIMITED.

AFIT-ENY-MS-21-M-329

DENSITY MEASUREMENTS OF NEUTRAL XENON USING MULTIPHOTON IONIZATION AND MICROWAVE SPECTROSCOPY IN A HALL EFFECT THRUSTER

Taylor J. Foy, BS

Committee Membership:

Dr. Carl Hartsfield
Chair

Maj Levi Thomas, PhD
Member

Dr. Robert Loper
Member

AFIT-ENY-MS-21-M-329

Abstract

A new dye laser and microwave scattering system for measuring low speed xenon particles was installed to characterize a commercially sourced 600 W Hall effect thruster. The new system uses multiphoton ionization and microwave spectroscopy to determine number density and velocity measurements of neutral xenon atoms in the plume of a Hall thruster. A study was conducted to ensure the new system will be able to accurately measure these neutrals in future work. The ultimate goal of this new system is to isolate and characterize the extra thrust produced in Hall Effect Thrusters due to finite volume vacuum chambers.

Acknowledgments

First, I would like to express my appreciation to the Air Force for allowing me take time out of my work schedule to complete my Master’s degree. To my family, I would like to thank them for their support and adherence to my request about not asking for thesis updates. Finally, I would like to thank my faculty advisor, Dr. Carl Hartsfield, for his guidance and support in this research. I am extremely grateful for all your help in this thesis process.

Taylor J. Foy

Table of Contents

Page

List of Figures

Page

List of Tables

List of Symbols

Symbol	
T	Thrust
$\dot{m}_p$	Mass Flow Rate of Propellant
u_{ex}	Exit Velocity
p_{ex}	Exit Pressure
p_0	Static Pressure
A_{ex}	Exit Area
ΔV	Change in Velocity
m_i	Initial Mass
m_f	Final Mass
I_{sp}	Specific Impulse
g_0	Acceleration Due to Gravity
θ	Angle
P_{jet}	Jet Power
q	ion charge
V_b	electric potential
M_i	mass of ion
η_m	mass utilization
$\dot{m}_\imath$	mass flow of ionized propellant
F	Force
E	Electric Field
B	Magnetic Field
v	velocity
ns	Nanosecond
mg	Milligram
u_e	drift velocity
B_r	Radial component of Magnetic Field
E_z	Axial component of Magnetic Field
I_H	Hall Current
n_x	Number density of species X
w	Plasma Width

V_d	Discharge Voltage
L	Larmor Radius
$v_\perp$	Perpendicular Velocity
v_n	Velocity of neutral particles
$\langle\sigma_i v_i\rangle$	Ionization reaction rate
r_e	Electron Larmor Radius
u_{th}	Thermal Velocity
ω_c	Larmor Frequency
m_e	Mass of Electron
k	Planck’s Constant
T_{eV}	Electron Temperature
l	Length of Magnetized Plasma Region
r_i	Ion Larmor Radius
u_i	Ion Velocity
m_i	Mass of Ion
Γ_n	Flux of Neutral Atoms
z	Distance Traveled Through Ionization Region
λ_i	Ionization Mean Free Path
Γ_{exit}	Flux of Neutral Atoms at Exit Plane
$\Gamma_{incident}$	Flux of Neutral Atoms from Anode
η_c	Cathode Efficiency
$\dot{m}_a$	Mass Flow Rate through Anode
I_c	Discharge Current
$u_{e,d}$	Electron Drift Velocity
A_o	Area of Cathode Orifice
Xe	Xenon
J	Joules of Energy
N	Newtons of Force
υ	Frequency
c	Speed of Light
λ	Wavelength
ΔE	Change in Energy
M^*	Excited State of Neutral Atom M

M^+	1st Ionization of Atom M
e^-	Electron
t_f	Final Time
P_{laser}	Power of Laser
t_{pulse}	Length of Time of the Laser Pulse
E_{pulse}	Energy of Laser Pulse
I_p	Photon Irradiance
A	Area of Laser Beam
W_i	Excitation Rate of Atoms
σ_i	Cross Sectional Area in the ith transition state
I_i	Laser Intensity
I_{peak}	Peak Laser Intensity
A_{ji}	Einstein Coefficient
$\Delta\nu_i$	Linewidth of transition
ϵ_0	Permittivity of Free Space
ν_0	Photon Frequency
f	Oscillator Strength
I_s^i	Saturation Intensity for the ith Transition State
τ_i	Relaxation Time in the ith State
ν_m	Total Collision Frequency
$\delta\nu$	Wavelength of Doppler Shift
F	Photon Flux
B_{eff}	Effective Recombination Rate
B_{dis}	Dissociative Recombination Rate
σ_{Pi}	Photo-ionization Cross Section
k_{convXe}	Rate Constant of Xe_2^+
k_e	Quenching Rate Constant
p_{photon}	Photon Momentum
v'	Atom Velocity After Bombardment

List of Abbreviations

Abbreviation	
AFIT	Air Force Institute of Technology
CEX	Change Exchange
DCM	4-Dicyanomethylene-2-Methyl-6-4-Dimethylaminostyryl-4H-Pyran
DUV	Deep Ultraviolet
LASER	Light Amplification by Stimulated Emission of Radiation
MATLAB	Matrix Laboratory
Nd-YAG	Neodymium-Doped Yttrium Aluminum Garnet
NIST	National Institute of Standards and Technology
ODE	Ordinary Differential Equation
RADAR	Radio Detection And Ranging
REMPI	Resonance-Enhanced Multiphoton Ionization
RGA	Residual Gas Analyzer
SFG	Sum Frequency Generation
SPASS	Space Propulsion Analysis and System Simulator
SPT	Stationary Plasma Thruster
TAL	Thruster with Anode Layer
UV	Ultraviolet

DENSITY MEASUREMENTS OF NEUTRAL XENON USING MULTIPHOTON IONIZATION AND MICROWAVE SPECTROSCOPY IN A HALL EFFECT THRUSTER

I. Introduction

Hall effect thrusters are a common form of spacecraft propulsion utilized by space systems from small satellites under 100 kilograms in low Earth orbit to large communications satellites of over 3000 kilograms in geostationary orbit. Hall thrusters produce small amounts of thrust by ejecting ionized atoms, normally xenon, at high velocities, and allow for more payload mass to be allotted when compared to chemical propulsion. A percentage of the propellent fed into the thruster is never ionized nor accelerated providing a loss of efficiency [1]. Understanding the un-ionized atoms can lead to efforts to minimize these loss terms, and production of more efficient thrusters.

A new system for measuring number density and particle velocities of neutral xenon utilizing multiphoton ionization and microwave absorption spectroscopy was employed to better understand gas distribution, mass utilization, and extra thrust produced from a Hall effect thruster in a vacuum chamber. This new measurement system will be used to measure the low speed neutral xenon particles in the plume of a commercially sourced Hall thruster that has been extensively tested at the Air Force Institute of Technology (AFIT). With validation of this new system and testing of multiple cases, particle velocity and number measurements may be obtained. The diagnostic system's ability to ionize xenon outside of the thruster also allows for evaluation of xenon flow reentry back into the thruster channel, a mechanism that increases thrust measurement in a vacuum chamber beyond achievable on-orbit values [2].

1.1 Background

Electrostatic thrusters have proven to be an important propulsion method for satellites in orbit and in long duration space missions due to their high specific impulse, reliability, and their flexibility in propellant. With their simplicity and low propellant use, they are a desirable choice for orbit correction and station keeping maneuvers. Hall effect thrusters are a type of electrostatic propulsion that utilize the Hall effect to ionize and propel individual atoms at high velocities using electrical power. Hall thrusters were first theorized in the United States in the 1960s [3], but were first used in orbit by the Soviet Union in 1971 on a weather satellite for orbit stabilization [4].

Several methods have been used to study the plume of electrostatic engines to better understand the plasma dynamics occurring. At AFIT, research has been performed on the Hall thrusters using Faraday probes [5], microwave interferometry [6] [7], and laser absorption spectroscopy [8]. Resonance Enhanced Multiphoton Ionization (REMPI) combined with coherent microwave scattering has been shown to achieve high resolution measurements of a stationary xenon gas [9], but has not been used to spatially resolve moving particles.

1.2 Motivation

Due to the high velocity particles propelled by ion engines and the low number density of plasma in the plume, measurements of the thruster are difficult. Faraday probes are a common plasma diagnostic method, although their physical presence in the thrust plume can lead to inaccurate results. These probes also get bombarded with high velocity ions leading to reduced probe lifetimes. Nonintrusive methods are desirable because there is no disturbance to the thruster plume while yielding high fidelity measurements. Spectroscopy is a common nonintrusive method to measure these plumes, but it requires precise configuration during experimental set-up and is more susceptible to environmental noise.

Extensive research has been done at AFIT to understand the characteristics of the Hall thruster using intrusive and non-intrusive methods. This research has focused on the high velocity plasma contained in the thruster plume, but has not looked directly into the particles that exited the thruster without being ionized.

There will always be a percentage of xenon particles that do not get ionized in the thruster channel and exit the thruster at low speeds. These low speed neutral particles do not contribute any meaningful thrust compared to the high velocity ionized particles, as their velocity is at least two orders of magnitude lower, and much less uniform in direction. A diagnostic using an ultra-violet laser system to ionize these neutrals, combined with microwave spectroscopy, is proposed as a method to spatially resolve the density and velocity of the neutral xenon. This system will allow for a better understanding of mass utilization and measurement of neutral xenon particles reentering the thruster due to being in a finite vacuum chamber. A microwave spectroscopy system will be measuring attenuation and doppler shifting of the REMPI ionized particles to determine number density and particle velocities. With proper validation of this new system a better understanding of mass utilization is possible, allowing for a more complete characterization of Hall thrusters. Also this research will show the impact of the propellant feed distribution to establish if the gas distribution is uniform or asymmetrical under different operating conditions.

1.3 Scope

The new REMPI and microwave spectroscopy system will be integrated in to the recently upgraded Space Propulsion Analysis and System Simulator (SPASS) vacuum chamber at the Air Force Institute of Technology for this research. To validate the diagnostic system functions, xenon propellant gas will be delivered through an unpowered thruster. Since the total mass flow of xenon is then known, diagnostic functions can be evaluated, and the uniformity of propellant distribution in the thruster measured. Testing this new system with the thruster powered will allow for comparison with Faraday probe results to verify mass utilization efficiency for the thruster. Running multiple experiments at various pressure points, generated by a controlled feed of xenon to the chamber, will allow for advanced modelling of thruster performance. Pairing this new system with the already available laser absorption spectroscopy system would all for full field measurements of singly ionized and neutral xenon atoms, although possibly not simultaneously.

1.4 Objective

The objectives of this research included:

1. Perform predictive analysis to establish the expected results from this system as installed
    a) Study the expected measured number density based on actual number density so that a correction can be established for the measured data

    b) Look at the impacts of aging laser dye and other components on this system to stablish thresholds for usability
    c) Analyze expected measurement limits to predict measurement limits and resolution for neutral velocity
2. Install the laser ionization and microwave system with enclosed beam path
3. Validate that the new system can accurately measure neutral xenon expelled from thruster in an unpowered condition for a known flow of neutral xenon
4. Obtain measurements with the thruster powered to verify previous mass utilization measurements
5. Develop methods to quantify the extra thrust produced by measuring xenon particles reentering the thruster

Eventually, this system will give the electric propulsion community a better understanding of the gas distribution of the anode/propellant feed manifold and an estimation of extra thrust produced by this thruster as a function of chamber pressure. Ideally, this knowledge will allow for refinements in Hall thruster design to increase mass utilization and allow satellite designers to have better estimates of on orbit performance.

II. Literature Review

Hall thrusters are a form of propulsion that expel ions at high velocities to generate thrust using electrical power. These thrusters enable spacecraft to travel faster and further than chemical rockets, while also offering precise control for station keeping and orbit raising maneuvers. In order to understand the theory behind this neutral detection system, a review of propulsion, laser, and spectroscopy topics will be derived. First, the theory behind chemical and electric propulsion are explained with a detailed analysis of Hall effect thrusters followed by a laser theory and how high intensity, high energy ultra-violet light can be produced. All elements are then tied together to explain how number density and velocity measurements are made using a new multiphoton ionization laser coupled with a microwave spectroscopy system.

2.1 Fundaments of Propulsion

In order for a body to accelerate, a force must be applied to set the body in motion. This force, called thrust, is produced by utilizing Newton's third law of motion that states every action has an equal and opposite reaction. In reaction engines such as jet engines, rocket engines, and Hall thrusters thrust is produced by ejecting propellant from the vehicle at high velocities. This propellant is stored onboard the vehicle and can be accelerated in a number of different ways. More propellant ejected from the engine during a given period of time will increase the amount of thrust, while ejecting propellant at higher velocities will give higher engine performance.

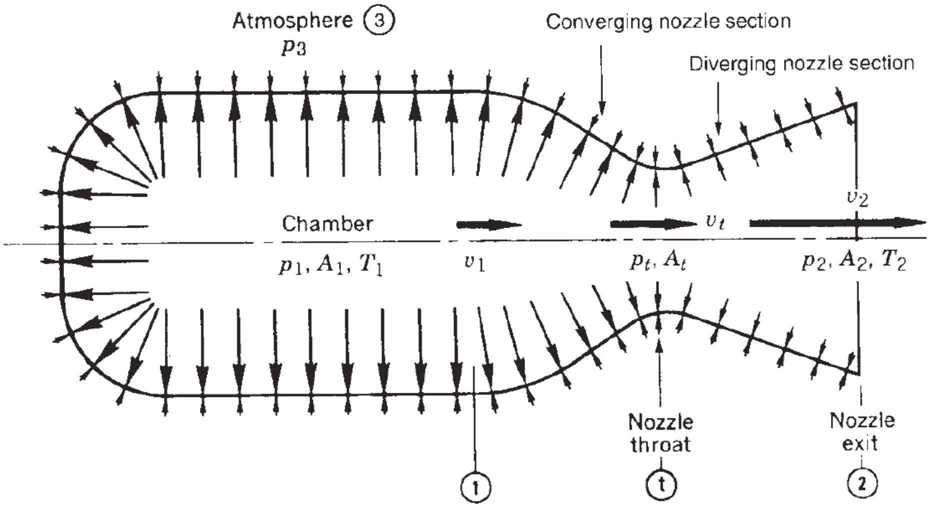

Figure 1. Basic operation of a chemical rocket [10]

Thrust is produced in a chemical rocket by combusting fuel and oxidizer that are contained within the vehicle, and accelerating it in a uniform direction and is defined by:

$$T = \dot{m}_p u_{ex} + (p_{ex} - p_0) A_{ex} \tag{1}$$

where $\dot{m}_p$ is the propellant mass flow rate exiting the rocket, u_{ex} is the velocity of the mass flow, p_{ex} and p_0 are the nozzle exit pressure and ambient pressure respectively, and A_{ex} is the nozzle exit area. From Equation 1, there are two contributions that are responsible for creating thrust. The first contribution, the mass flow rate times exit velocity, results from the chemical reaction of combustion. The hotter fuel can be burned will increase pressure within the chamber and will lead to higher potential energy, creating the potential for higher exhaust velocity and more thrust. The second contribution to thrust comes from the geometry of the nozzle. The converging-diverging nozzle chokes the flow from the combustion chamber down at the throat accelerating the flow to a Mach number of 1. The flow entering the diverging section is allowed to expand the combusted gases, accelerating them in the process to Mach numbers well over 1, and very high velocities.

Since all propellent must be carried with a vehicle, propellant is a predominant limiting factor in a spacecraft's lifetime. Propellant mass can be related to the total change in velocity of the rocket, called ΔV, using Tsiolkovsky's ideal rocket equation [10]:

$$\Delta V = u_{ex} ln \frac{m_i}{m_f} \tag{2}$$

where m_i is the initial spacecraft mass and m_f is the final mass. Typically, the final mass is defined as:

$$m_f = m_{payload} + m_{structure} + m_{power\ plant} \tag{3}$$

The ideal rocket equation also shows that gas exiting the thruster at higher velocity will require less fuel to be consumed to create the same change in velocity.

Another measure of engine performance is called specific impulse, I_{sp}, defined as:

$$I_{sp} = \frac{u_{ex}}{g_0} = \frac{T}{\dot{m}_p g_0} \tag{4}$$

where g_0 is the acceleration due to gravity at sea level, 9.807 m/s^2. Specific impulse is a measure of how effectively an engine converts its fuel into kinetic energy, and is inversely proportional to specific fuel consumption [10].

The final quantity of an engine that will need to be defined is the jet power, P_{jet}. Jet power is the time derivative of kinetic energy of the exhaust and is defined as:

$$P_{jet} = \frac{1}{2}\dot{m}_p {u_{ex}}^2 = \frac{T^2}{2\dot{m}_p} \tag{5}$$

Jet power is proportional to the square of exit velocity of the propellant, and shows that increasing exit velocity creates greater propulsive effectiveness and increases jet power.

2.2 Electric Propulsion

Another method of propulsion involves increasing exit velocity by an order of magnitude when compared to chemical rockets at the expense of thrust. Chemical rockets use a reaction within the fuel to break chemical bonds to release energy that is converted into kinetic energy. The available energy is thus limited by the fuels used, and can create exit velocities up to about 4-5 km/s. Electric propulsion thrusters accelerate individual particles to high velocities using electric fields and do not rely on chemical reactions to create kinetic energy, instead separating the propellant from the energy source. This separation means exit velocities are dependent on electrical power and allows for greater exit velocities. Electric propulsion engines can produce exit velocities above 30 km/s [1].

Specific Impulse (sec)	Maximum Temperature (C)	Thrust-to-Weight Ratio	Propulsion Duration	Specific Power (kW/kg)	Typical Working Fluid	Status of Technology
200-468	2500-4100	10^{-2}-100	Seconds to a few minutes	10^{-1}-10^{3}	Liquid or solid propellants	Flight Proven
194-223	600-800	10^{-2}-10^{-1}	Seconds to minutes	0.02-200	N_2H_4	Flight Proven
150-300	20000	10^{-4}-10^{-2}	Days	10^{-3}-10^{-1}	H_2 , N_2H_4	Flight Proven
280-800	-	10^{-4}-10^{-2}	Days	10^{-3}-1	H_2 , N_2H_4 , NH_3	Flight Proven
700-2500	-	10^{-6}-10^{-4}	Weeks	10^{-3}-1	H_2 , Solid for PP	Flight Proven
1220-2150	-	10^{-4}	Weeks	10^{-1}-0.5	Xenon	Flight Proven
1310-7650	-	10^{-6}-10^{-4}	Months, Years	10^{-3}-1	Xenon	Flight Proven
400-700	1300	10^{-3}-10^{-2}	Days	10^{-2}-1	H_2	In Development

Figure 2. Performance parameters for various spacecraft propulsion options [10]

Electric propulsion is generally separated into three families differentiated by their methods of accelerating the propellant. Electrothermal thrusters are the first family, and use electrical power to heat a gas to raise its temperature and accelerate it through a nozzle, similar to chemical rockets. The second family of electric propulsion consists of electrostatic thrusters, that create ions inside of a chamber and accelerate them through an electric field using the Coulomb force. The last family consist of electromagnetic thrusters, where ions are accelerated by electric and magnetic fields utilizing the Lorentz force. Electrostatic and electromagnetic thrusters have the benefit of being flexible in propellent, many of which are not as toxic as chemical propellants. Typically, xenon is chosen due its high atomic mass, its ease of ionization of the fifth shell of valence electrons, its high density, and because it is an inert gas. Krypton is also monatomic gas that is commonly used as a propellent in ion engines and potentially provides a higher I_{sp} due to its lower atomic weight when compared to xenon. However, krypton has a slightly higher ionization potential and leads to generally lower propulsion efficiencies [11]. In chemical rockets, propellants with low molecular masses will have higher I_{sp} due to the isentropic relations, with liquid hydrogen and oxygen giving the highest theoretical I_{sp} [10] among common propellant combinations. However, in electrostatic and electromagnetic thrusters, higher atomic mass particles provide thrust due to Newton's second law, and higher specific impulse due to improved mass utilization.

Electric propulsion systems must also include systems to convert low voltages used in the spacecraft bus supplied by solar power or nuclear reactors into higher voltages required by the thrusters. These systems can lead to more of the mass budget being budgeted towards the engine instead of payloads.

Due to the low amount of thrust typically produced by electric propulsion, orbital maneuvers must be conducted differently than with chemical rockets. Where a chemical rocket can conduct almost impulsive burns, lasting on the order of 1-2 minutes for most large orbit maneuvers, electric propulsion must constantly be running over long periods of time (days to weeks) to prove the same amount of ΔV. Figure 3. Hohmann Transfer Maneuver vs Continuous Electric Propulsion shows orbital insertion via a typical Hohmann transfer orbit compared to a high thrust electric propulsion spiral orbit. Many different orbital maneuvers can be used to reach a target orbit, and engineering decisions are needed to determine what propulsion systems are best suited for the mission. The higher I_{sp} of electrical propulsion thrusters mean less propellant is needed to reach the target, but will take longer to reach the intended orbit. If time is not of the essence, less mass allocated for propellant means that there can be greater payload mass. Electric propulsion is also a good choice for satellite station keeping, as their low thrust provide fine controllability.

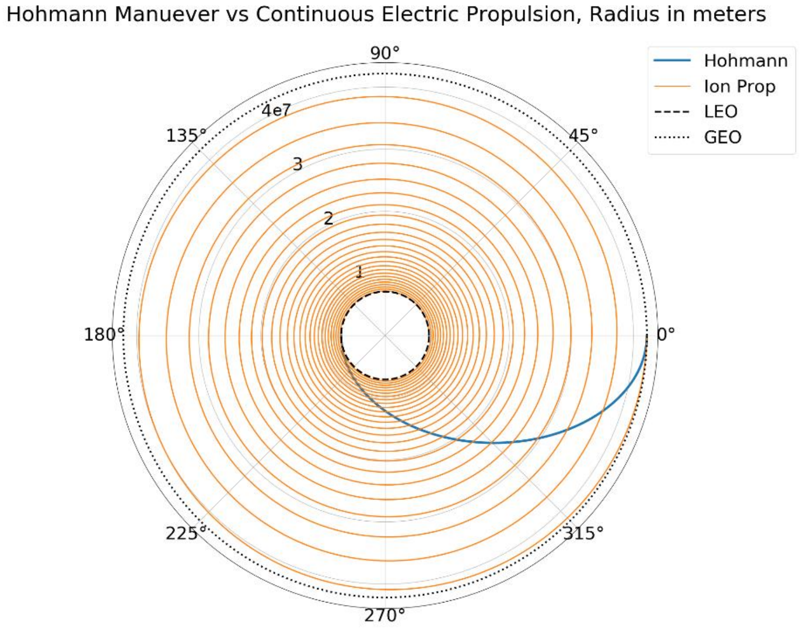

Figure 3. Hohmann Transfer Maneuver vs Continuous Electric Propulsion

2.3 Electrostatic Propulsion

As mentioned in Section 2.1, electrostatic thrusters create thrust by generating then accelerating ions with an electric field. Different methods of generating the electric field have been implemented, with gridded ion thrusters and Hall thrusters consisting of the majority of designs. Thrust provided by an electrostatic thruster is only generated by the mass flow rate of ionized propellent. Since the pressures are very low, the nozzle expansion from Equation 1 can be ignored:

$$T = \dot{m}_p u_{ex} \tag{6}$$

The exit velocity of ions is a function of electric potential, V_b, ion charge, q, and the atomic mass of the ion, M_i and is defined as:

$$u_{ex} = \sqrt{\frac{2qV_b}{M_i}} \tag{7}$$

Various efficiencies reduce the actual thrust production of an electrostatic propulsion system. Plume divergence, electrical efficiency, and mass utilization are key sources of losses on electrostatic thrusters. Mass utilization η_m is a key quantity in this research and is defined as the ratio of propellent that is ionized to the propellent fed into the thruster:

$$\eta_m = \frac{\dot{m}_i}{\dot{m}_p} \tag{8}$$

Specific impulse for electrostatic thrusters can then be redefined as:

$$I_{sp} = \frac{u_{ex}}{g_0}\eta_m \tag{9}$$

2.4 Hall Effect Thrusters

Hall effect thrusters are a moderate specific impulse form of electrostatic propulsion that use a magnetic field to trap electrons into azimuthal motion while a neutral gas is injected into a thruster channel [12]. The neutral particles are then impacted by high velocity electrons and ionized. The high electron density in the Hall current compresses the electric field between the external cathode and the anode at the back of the Hall thruster ionization channel, resulting in a high, nearly axial field in the exit region of the Hall thruster. This electric field accelerates the ions to extremely high velocities to generate thrust.

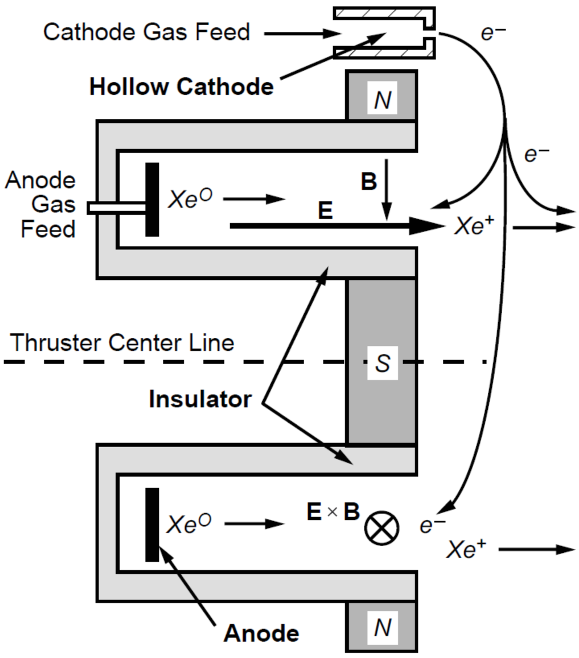

Figure 4. Hall Effect Thruster Cross Section [1]

Two designs of Hall thrusters have been developed, Stationary Plasma Thrusters (SPT) and Thrusters with Anode Layer (TAL). Both designs have the same basic operation and acceleration methods, with the difference being that TALs contain an extended anode section that protrudes into the thruster channel to shorten the electric field region in the channel [1]. Thrust is produced in Hall thrusters by the Lorentz Force defined as:

$$\vec{F} = q(\vec{E} + \vec{v} \times \vec{B}) \tag{10}$$

with the majority of the force being produced by the electric field component. Hall thrusters are classified as electrostatic propulsion even though electromagnetism is utilized. This is because the accelerating force due to magnetism is negligible compared to the electrostatic force and is normal to the electrostatic force, resulting in a force in the azimuthal direction.

Many of the electrons used to ionize and accelerate the propellant are emitted by an external hallow cathode are attracted towards the anode at the back of the ionization channel, but are trapped into azimuthal motion by the magnetic field. The drift velocity of these electrons is defined as u_e:

$$u_e = \frac{\boldsymbol{E} \times \boldsymbol{B}}{B^2} \approx \frac{E_z}{B_r} \tag{11}$$

where the B_r indicated the radial component of the magnetic field, and E_z indicates the axial component. This electron drift creates a current known as the Hall current defined as:

$$I_H \approx n_e e w \frac{V_d}{B} \tag{12}$$

where n_e is the number density of electrons, e is the charge of an electron, w is the plasma width, V_d is the discharge voltage. By balancing the Lorentz Force with centripetal force, the Larmor radius is defined:

$$L = \frac{m v_\perp}{|q| B} \tag{13}$$

For Hall thrusters, the Larmor radius can be defined as:

$$L = \frac{v_n V_d w}{I_H \langle \sigma_i v_i \rangle B} \tag{14}$$

where v_n is the velocity of the neutral particles, and $\langle \sigma_i v_i \rangle$ is the ionization reaction rate coefficient and is tabulated for Xenon in [1]. The ionization reaction rate is a function of electron temperature. In order for the electrons to be captured by the magnetic field, the following criteria must be met:

$$r_e = \frac{u_{th}}{\omega_c} = \frac{m_e}{eB}\sqrt{\frac{8kT_{eV}}{\pi m_e}} = \frac{1}{B}\sqrt{\frac{8m_e}{\pi e}T_{eV}} \ll\ l \tag{15}$$

where r_e is the electron Larmor radius, and *l* is the depth of the magnetized plasma region. As electrons are emitted by the cathode, they will travel along the magnetic field lines in a spiral movement. If the thruster channel isn't long enough for electrons to be captured by the magnetic field, the electrons will simply flow into the anode completing the circuit. The reduction in electron mobility also leads to the magnetic and electric fields becoming the strongest at the thruster exit plane [1]. Similar to the electron Larmor radius criteria, the ion Larmor radius r_i must be larger than the thruster channel length. This condition is necessary for ion acceleration by the electric field and is defined as:

$$r_i = \frac{u_i}{\omega_c} = \frac{m_i}{eB}\sqrt{\frac{8eV_B}{m_i}} = \frac{1}{B}\sqrt{\frac{8m_i}{e}V_B} \gg\ L \tag{15}$$

As neutral particles are injected into the ionization region of the thruster channel, the number of neutral particles will decrease over time due to the electron collisions. This rate is defined by:

$$\frac{dn_n}{dt} = -n_n n_e\langle\sigma_i v_i\rangle \tag{16}$$

where n_n and n_e is the number density of neutrals and electrons respectively. By introducing the velocity of the neutral particles, the following substitution can be made and Equation 16 can be written as:

$$\mathit{\Gamma}_n = n_n v_n \tag{17}$$

Substituting Equation 17 into Equation 16 gives:

$$\frac{d\Gamma_n}{\Gamma_n} = -\frac{n_e\langle\sigma_i v_i\rangle}{v_n}dz \tag{18}$$

Equation 18 has the solution for ionization as a function of distance traveled through the ionization region:

$$\Gamma_n(z) = \Gamma(0)e^{-z/\lambda_i} \tag{19}$$

where z is defined as the distance from the beginning of the ionization region and λ_i is the mean free path. The distance a neutral particle will travel before becoming ionized is called the ionization mean free path, and is defined as:

$$\lambda_i = \frac{v_n}{n_e\langle\sigma_i v_i\rangle} \tag{20}$$

If the ion Larmor radius is substituted into Equation 19, a condition can be derived to reach any specific level of ionization.

$$L = \lambda_i \; - \; ln(1 - \frac{\Gamma_{exit}}{\Gamma_{incident}}) \tag{21}$$

where Γ_{exit} is the neutral flux at the exit plane of the thruster and $\Gamma_{incident}$ is the flux of neutrals coming from the anode. Using Equation 21 with a desired ionization percentage, an ion Larmor radius can be found.

2.4.1 Hollow Cathodes

The electrons captured by the magnetic field are used to ionize the propellant are provided by a cathode that is typically externally mounted. Hollow cathodes are commonly paired with ion engines due to lower operating voltages and higher current emissions compared to conventional cathodes [13]. In a hollow cathode, an insert that is placed inside of a tube is surrounded by a heating mechanism. When this insert is heated to an emissive temperature, electrons will be emitted into the cavity of the cathode. A small portion of the propellent is diverted into the cavity and is ionized by the emitted electrons, creating a steady electron discharge that then exits the cathode through the orifice. A positively biased keeper electrode may also be included to enclose the cathode that helps to start electron discharge and shield the cathode from erosion via ion bombardment. A diagram of a typical hollow cathode is shown in Figure 5. Hollow Cathode Diagram . Cathodes also provide electrons to neutralize ions in the thruster plume.

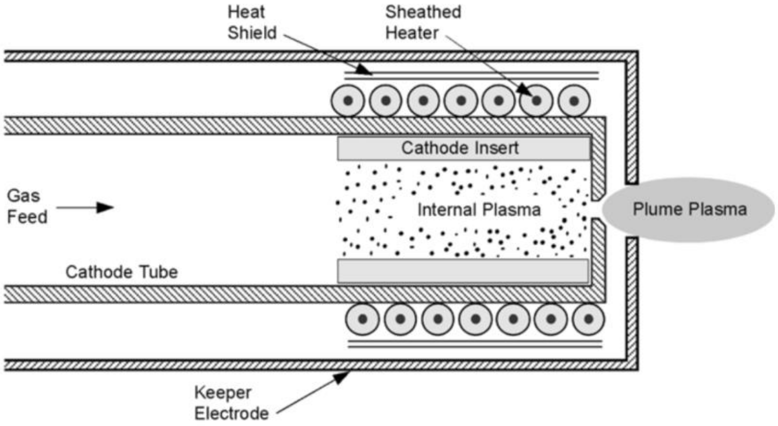

Figure 5. Hollow Cathode Diagram [1]

A measure of cathode efficiency can be defined in terms of the total mass flow through the anode m_a versus the cathode m_c:

$$\eta_c = \frac{\dot{m}_a}{\dot{m}_p} = \frac{\dot{m}_a}{\dot{m}_a + \dot{m}_c} \tag{22}$$

The discharge current through the orifice of a cathode is defined as:

$$I_c = n_e e u_{e,d} A_o \tag{23}$$

where n_e is the plasma density, $u_{e,d}$ is the electron drift velocity and A_o is the area of the cathode orifice. Erosion due to ion bombardment, also called sputtering, is an issue that arises in hollow cathodes over long periods of use, and is one of the primary life-limiting factors with respect to ion engines. Inside of the hollow cathode, sputtering will increase cross sectional orifice area, and outside of the cathode high velocity ions in the thruster plume can cause sputtering on the keeper electrode. The cathode insert that is in direct contact with the plasma is also subject to erosion, and also will limit the lifetime of hollow cathodes.

2.4.2 Hall Thruster Plumes

The plume of a Hall thruster contains a number of species of particles. The majority of particles in the plume are high kinetic energy singularly charged xenon ions. A small percentage of the charged ions may also be doubly and triply charged xenon atoms with percentages shown in Table 1 Hall Thruster Ionized Xenon Species Fractions at 300V Discharge were experimentally derived [5]. As discussed earlier, the plume will also contain low kinetic energy neutral xenon atoms that were never ionized nor accelerated. Another species contained in the plume of Hall thrusters result from charge exchange reactions (CEX). These reactions occur when a high speed ion collides with a low speed neutral, resulting in the low energy neutral becoming ionized and the high speed ion gaining an electron and becoming neutral [1] [14]. Trace particles in the plume may also include sputtering materials from the thruster channel or the hollow cathode.

Table 1 Hall Thruster Ionized Xenon Species Fractions at 300V Discharge [5]

Species	Fraction
Xe II	0.825
Xe III	0.093
Xe IV	0.072

Xe V	0.01

Due to testing Hall thrusters in a finite volume vacuum chamber, high velocity particles ejected from the thruster will impact the chamber walls and diffuse around the chamber unpredictably. A percentage of these neutral particles will eventually find themselves moving back into the thrust channel, and will again be ionized and propelled from the engine. This phenomenon produces slightly larger thrust measurements for Hall effect thrusters in vacuum chambers than actual performance on orbit [14]. According to Equation 1, thrust should decrease as ambient pressure increases. Figure 6. Chamber Pressure Effects on Thrust of Hall Thruster shows the results from Reference [15], where this phenomenon was observed, resulting in thrust increasing by around 5% as the chamber pressure increased.

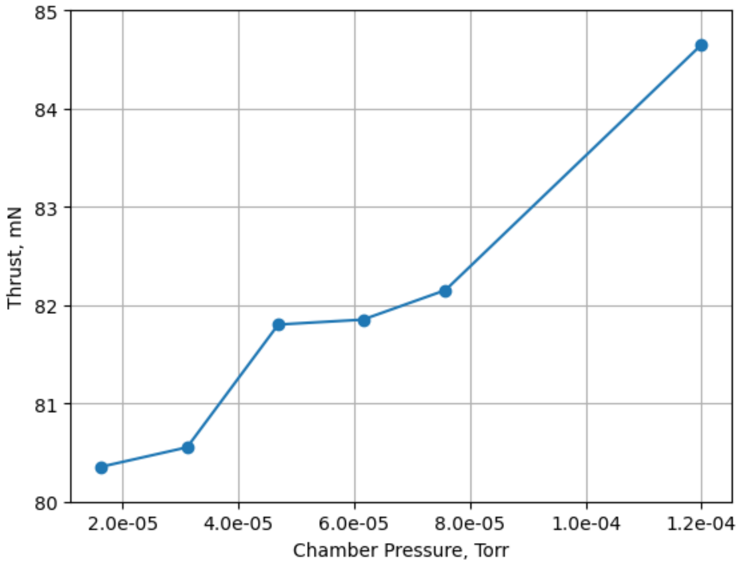

Figure 6. Chamber Pressure Effects on Thrust of Hall Thruster

2.5 Plasma Diagnostics

Getting accurate full field measurements of Hall thruster plumes has been of interest since their development. Understanding the harmonics generated by the plasma interactions in the thruster channel, experimenting with different fuel mixtures, and trying to improve mass utilization are additional active areas of research in electric propulsion. In general, there are two primary methods of measuring particles inside the thruster channel and in the thruster plume: intrusive and nonintrusive. Common forms of intrusive measurements are Faraday probes and E x B probes, that utilize a physical probe to measure the ion charge flux at a particular location. Probe measurements offer a simple method to determine particle exit velocities and thrust produced. The physical presence of a probe may lead to instability modes within the thruster and therefore inaccurate measurements [8]. These probes are also under constant ion bombardment, and will degrade over time. Nonintrusive methods avoid these issues, but require precise calibrations and experimental set up. A common nonintrusive method to study plasma is spectroscopy, that looks at the interaction between matter and electromagnetic radiation.

2.5.1 Laser Fundamentals

Light Amplification by Stimulated Emission of Radiation, or LASER, is a system that produces a narrow bandwidth of coherent light using optical amplification. The light consists of many photons, with the energy per photon defined as:

$$E = hv \ = \ hc/\lambda \tag{24}$$

where E is the energy of a photon in Joules, h is Planck's constant, and ν is the frequency of the photons emitted, c is the speed of light in meters per second, and λ is the wavelength of the photon. Lasers can be designed to operate in a steady-state mode that will emit a constant stream of photons per second. Lasers may also operate by sending pulses of photons within a certain timestep before needing to generate more photons to be sent in the following pulse.

The photons produced in the laser are produced using the stimulated emission of atoms. When a photon with a particular wavelength or energy produced by another source is absorbed by an electron in a ground state orbiting an atom, it will enter an excited state. The different quantized excited states of different atoms are well known through experimental findings [16]. The excited electron will try to shed this excess energy and return down to its ground state quickly, and can do this either spontaneously or be stimulated by another photon. Spontaneous emission will produce a photon with energy equal to the energy difference between the excited and ground states in a random phase and direction. If the excited electron interacts with another photon, it will produce a photon "copy" at the same wavelength and phase of the incoming photon. A diagram showing this process is shown in Figure 7. Stimulated Emission .

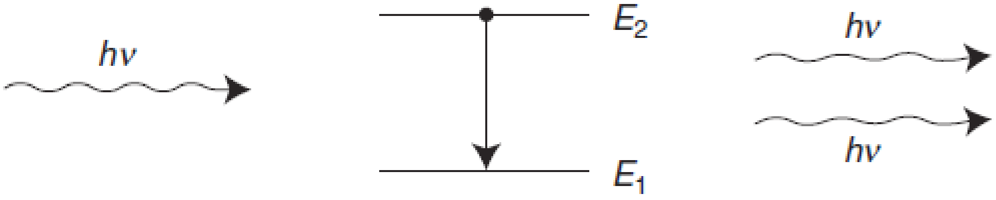

Figure 7. Stimulated Emission [17]

The equation governing this stimulated emission is:

$$E_2 - E_1 = \Delta E = h\nu \tag{25}$$

where E_2 denotes the energy of an excited atom, and E_1 denotes the ground energy state.

Lasers typically contain three components: an energy source, a gain medium, and an optical resonator. The energy source, often called a pump, provides energy in the form of electric current or photons into the gain medium to generate stimulated emission. The material in the gain medium is specifically chosen to absorb and emit photons at a particular frequency, amplifying the light produced via stimulated emission. An array of mirrors, called an optical resonator, is set up to reflect the light through the gain material in order to amplify the number of photons produced. An example of an optical resonator can be seen in Figure 9. Dye Laser Beam Path. Finally, the light reaches a semi-transparent lens that allows some of the photons through and out of the laser system. Laser light has the unique property of being high intensity and coherent, meaning that photons produced have the same phase, polarity, and a very small bandwidth centered around the desired wavelength. A black body emits radiation broadly across a long number of wavelengths according to Planck’s law, but laser emission has an extremely narrow bandwidth (called the laser linewidth) typically on the order of 2 picometers [18]. A visualization of this difference is shown in Figure 8. Emission Spectrum of a Blackbody Compared to a Laser.

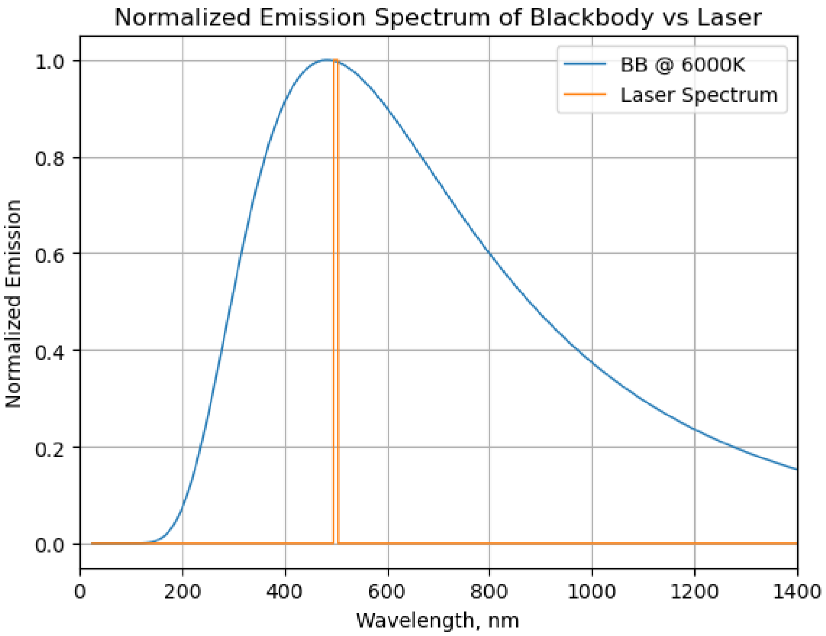

Figure 8. Emission Spectrum of a Blackbody Compared to a Laser

2.5.2 Dye Lasers

Dye lasers contain the same basic components of a traditional laser system, but use an organic mixture of molecules as a gain material. Depending on the dye used, different wavelengths will be output from the dye laser. These types of lasers are also ideal for applications where fine tuning of the laser is needed, as the output of dye lasers is a broader emission curve ranging between 1-6 nm wide [17]. These lasers are available in both pulsed and steady state varieties.

Figure 9. Dye Laser Beam Path [19]

The energy source used to pump a dye laser is typically a solid-state laser operating in optical wavelengths. Photons from the pump laser will be absorbed by the organic molecules within the dye, putting the molecule in an excited state. Unlike the gain medium in solid-state systems, additional energy is put into the molecules above the lowest level of a particular state. The molecules very quickly decay into the lowest level of this vibrational state, typically within the picosecond range [17]. The molecule then emits a photon equal in energy to the difference between the lowest level vibrational state and the initial state. This process is the result of the Franck-Condon Principle, shown in Figure 10. Stimulated Emission in Dye Laser and Figure 11. Franck-Condon Principle [17].

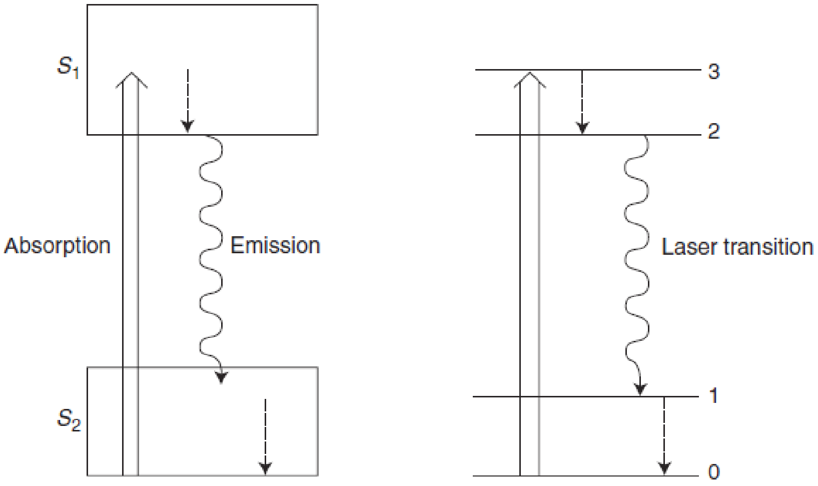

Figure 10. Stimulated Emission in Dye Laser [17]

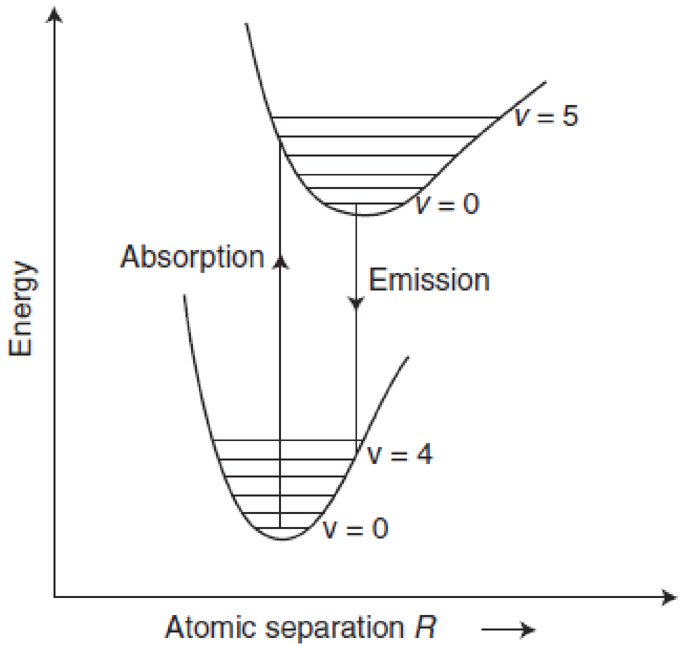

Figure 11. Franck-Condon Principle [17]

The result of the Frank-Condon principle is that the frequency of the emitted photon will be shifted slightly from the absorption photon. The absorption process occurs at a higher frequency, undergoes a shift, then emits at a lower frequency. This shift is called the Stokes shift, and is fundamental to laser systems.

2.5.3 Sum Frequency Generation

While high powered laser light (containing a high number of photons) may be desired, a reduction in the wavelength (increasing the energy per photon) may also be required. This reduction can be achieved with Sum Frequency Generation (SFG). This method for increasing the energy per photon is achieved by passing the laser light through a nonlinear optical crystal and is a second order nonlinear process that exploits the modification of optical properties of a material in the presence of high intensity light [20]. In this phenomena, two photons are “combined” to generate a new photon with a frequency equal to the sum of the initial photons:

$$hv_3 = hv_1 + hv_2 \tag{26}$$

SFG is caused by the polarization within a media responding non-linearly to an applied electric field. The nonlinear crystal can be placed either within the laser optical path or external to the laser system [17]. If the two photons have the same frequency, the process is called Second Harmonic Generation. In this research, two laser beams of different wavelengths will be combined using SFG to produce light in the ultra-violet (UV) region. Figure 12. Sum Frequency Generation Diagram shows a diagram of the process of SFG.

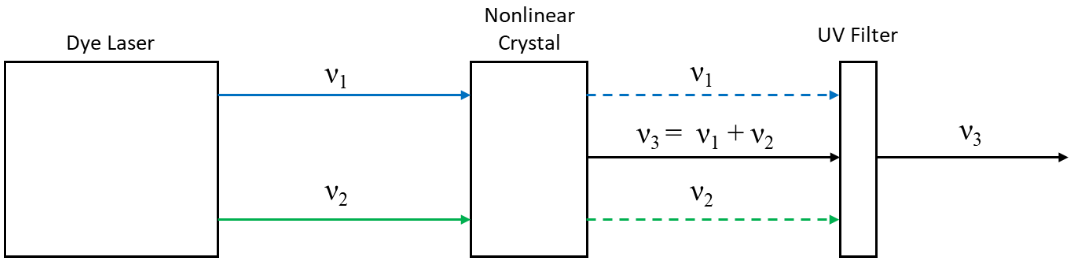

Figure 12. Sum Frequency Generation Diagram

Typically, a filter is placed after the nonlinear crystal to only allow the desired wavelengths of photons through, preventing extraneous photons from the dye laser that were not combined from proceeding. Dye lasers that utilize SFG have the advantages of longer dye lifetimes, and have smaller spectral bandwidth when compared to systems using SHG [21].

2.5.4 Resonance Enhanced Multiphoton Ionization

Ionization within a Hall thruster occurs when high speed electrons traveling in a circular path around the thruster channel collide with neutral propellent atoms. The electrons contain sufficient kinetic energy to free a valence electron from the neutral atom. Ionization can also occur in photon-neutral collisions, called photoionization. From Equation 24, the energy of contained in a photon is directly proportional to the frequency of the photon. Photoionization takes the form:

$$M + h\upsilon \rightarrow M^{*} \rightarrow M^{+} + e^{-} \tag{27}$$

where M denotes the neutral atom, hv is the energy of and incoming photon, M* shows the atom in an excited state, M^+ is the ion, and e^- is the electron freed from the neutral. The ionization energy for a xenon atom is 12.1298eV, equating to 1.94×10^{-18} Joules [22].

Since it may be impractical to produce individual photons with enough energy to ionize an atom, multiphoton ionization can be used. Due to atom’s tendency to absorb photons, an accumulation of energy due to multiple absorptions is possible. Resonance Enhanced Multiphoton Ionization is a technique that uses a high powered laser to place the atom into an excited state, leading to ionization with further photon absorption. Typically, the photons used in REMPI are all of the same wavelength, and their individual energies add together. The atom will want to shed the excess energy that placed it into the excited state very quickly in the form of a photon. In order to prevent the unwanted relaxation, either a steady state laser or pulsed lasers with the capability to produce pulses within the picosecond range rather than the more standard nanosecond range are required [23]. If the last photon to be absorbed and cause the ionization imparts more energy into the atom, this excess electric energy will be shed.

For a xenon atom, REMPI is typically achieved by using three photons. The first two photons place the atom into excited state, and must be absorbed simultaneously [16]. The third photon is absorbed before the atom decays into its ground state, causing ionization. Conventionally this is notated as a 2+1 REMPI scheme, and is shown in Figure 13. 2+1 REMPI Scheme.

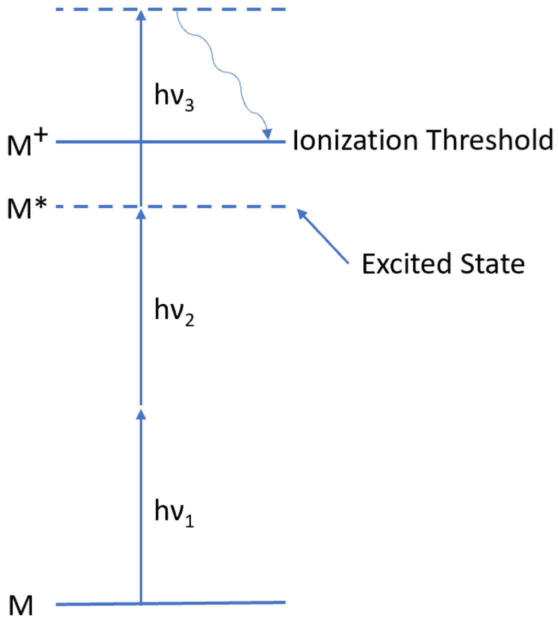

Figure 13. 2+1 REMPI Scheme

The number of photons per pulse produced by a laser is defined by the energy in a laser pulse divided by the energy of a photon at the laser frequency:

$$n_{photons} = \frac{E_{pulse}}{h\nu} = \frac{\int_0^{t_f} P_{laser} dt}{h\nu} \tag{28}$$

where $n_{photons}$ is the number of photons produced in a pulse, E_{pulse} is the energy of a laser pulse.

By rearranging Equation 28 and assuming a time-invariant laser, the power of laser can be found:

$$P_{laser} = \frac{n_{photons} h\nu}{t_{pulse}} \tag{29}$$

Due to the high intensity needed to produce REMPI, the laser beam must be focused into a smaller area. The number of photons per unit are can be defined with:

$$I_p = \frac{P_{laser}}{A} = \frac{n_{photons} h\nu}{t_{pulse} A} \tag{30}$$

where I_p is the photon irradiance (photons per unit area).

The excitation rate of atoms is given by:

$$W_i = \sigma_i I_i \tag{31}$$

where i denotes the transition state, W is the excitation rate in units of photons per second, σ is the cross-section area, and I is the laser intensity in photons per cm^2 per second. The cross section is defined by:

$$\sigma_i = \frac{\lambda^2}{2\pi} \frac{A_{ji}}{\Delta\nu_i} \tag{32}$$

where A_{ji} is Einstein coefficient from state i to j, λ is the wavelength of the photon causing excitation, and $\Delta\nu_i$ is the linewidth of the transition. The Einstein coefficient is a measure of the probability of transition between two particular states, i and j [24] if there is only one allowed absorption transition and is defined as:

$$A_{ji} = \frac{1}{4\pi\epsilon_0} \frac{2e^2\nu_0^2}{mc^3} f \tag{33}$$

where ϵ_0 is the permittivity of free space, ν_0 is photon frequency, and f is called the oscillator strength [17]. Einstein coefficients have been experimentally derived and compiled by NIST [22].

When looking at the 2+1 REMPI scheme, the following derivation can be used to determine the required laser intensity [25]. Since two photons need to be absorbed simultaneously, the excitation rate scales as the intensity squared [16], and Equation 31 becomes:

$$W_1 = \sigma_1 I_1^2 \tag{34}$$

where the subscript denotes the first transition from the ground state of the atom to the excited state. The laser intensity must be higher than the saturation intensity (I_s^1) for the first transition state:

$$I_1 > I_S^1 = (2\sigma_1\tau_1)^{-1} \tag{35}$$

where τ_1 is the relaxation time for the first state. Assuming that the relaxation time is only determined by radiative decay, τ_1 can be replaced with A_{21}^{-1}.

From the excited state to ionization transition, the required laser intensity is defined by:

$$I_2 > I_S^2 = (\sigma_2\tau_1)^{-1} = \frac{\sigma_1}{\sigma_2} 2\, I_S^1 \tag{36}$$

From Equation 36, it can be seen that the required intensity for saturation increases by:

$$I_p \propto 2^{n_{photons}-1} \tag{37}$$

2.5.5 Microwave Spectroscopy

Microwave spectroscopy is a non-intrusive method of obtaining field measurements of a gas and is typically used to measure rotational energy states of molecules [26]. The board spectrum incapsulated in the microwave bands, typically defined as radiation between 300 MHz and 300 GHz [27], allow for specific tuning depending on the molecule that is being studied.

As the microwaves exit a high gain horn transceiver and pass through the thruster plume, the waves of radiation will interact with the electrons freed during ionization. This interaction with free electrons will lead to microwave scattering with some energy reflected back towards the receiver. A photodiode is also needed to measure the baseline laser energy, and by comparing this signal to the signal from the scattered microwaves, a number density can be calculated. The reflected energy can be related to the number of electrons freed by:

$$E_{signal}(t) \propto \frac{n_e(t)}{v_m(t)} \tag{38}$$

where v_m is the total collision frequency.

The relationship between the reflected signal and laser intensity has been shown to be nearly linear [28]. Nonlinearities in this relationship arise from variations in collision frequencies and other factors including a depolarization factor [29]. This is same process used in conventional radar systems to detect stationary or moving objects. This method, called Radar REMPI, has been successfully used to obtain number density measurements of the created ions [9]. A diagram of this process is shown in Figure 14. Illustration of Microwave Scattering Setup to Measure Number Density of Neutrals in a Hall Thruster Plume.

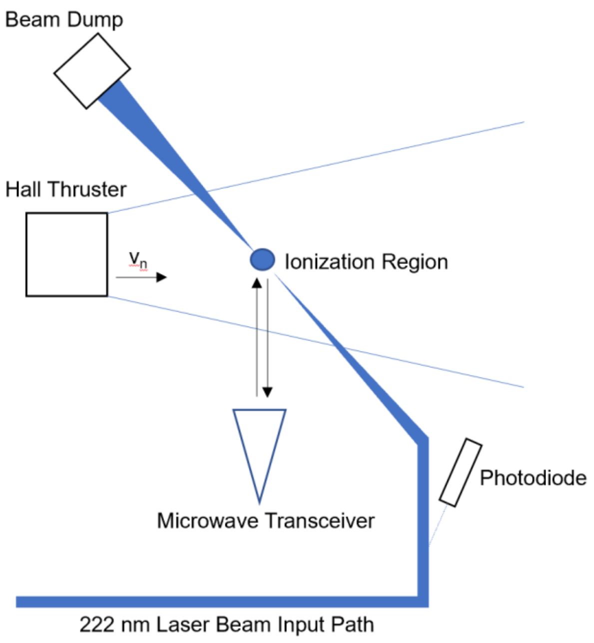

Figure 14. Illustration of Microwave Scattering Setup to Measure Number Density of Neutrals in a Hall Thruster Plume

To measure the velocity of ions, the same microwave source can be used by placing the microwave transceiver at an angle of incidence to the velocity vector of the neutrals. By comparing the wavelength of the signal to the wave form created by the microwave source, particle velocities can be calculated by measuring the Doppler shift if the source microwaves have a component parallel to the particle velocities. This method was successfully used to measure high velocity ions using a laser absorption spectroscopy at 824 nm [8]. A second transceiver placed orthogonal to the initial horn can be used to increase spatial resolution of the velocity measurements. The doppler shift is defined by:

$$\delta\nu = \nu\frac{v_n}{c} \tag{39}$$

where $\delta\nu$ is the wavelength of the shifted signal due to the Doppler effect, ν is the wavelength of the source microwave signal, and v_n is the velocity of the neutral atom (in the axial direction). Solving Equation 39 for the neutral atom velocity and accounting for the microwave source being at an angle θ to the thruster plume, the equation becomes:

$$v_n = c\,\frac{\delta\nu}{\nu} \cos\theta \tag{40}$$

III. Methodology

The Air Force Institute of Technology’s SPASS laboratory was used as the primary location for this research. This laboratory has been used for numerous experiments in the field of electric propulsion and houses the largest vacuum chamber at AFIT. The recent upgrades to the chamber and the installation of the new laser system bring new capabilities to this already dependable laboratory.

Section 3.1 contains the operation of the chamber, Section 3.2 details the installation of the dye laser system, Section 3.3 discusses the installation and operation of the microwave scattering system, Section 3.4 details the thruster traverse, and Section 3.5 outlines the testing conditions.

3.1 Laboratory

The installation of the new dye laser and microwave system took place at AFIT’s SPASS lab. The SPASS laboratory vacuum chamber is 1.8 meters in diameter, and 3.75 meters in length and has been utilized for multiple Hall thruster experiments. The chamber itself is made of stainless steel comprised of three sections of 1.25 meters in length.

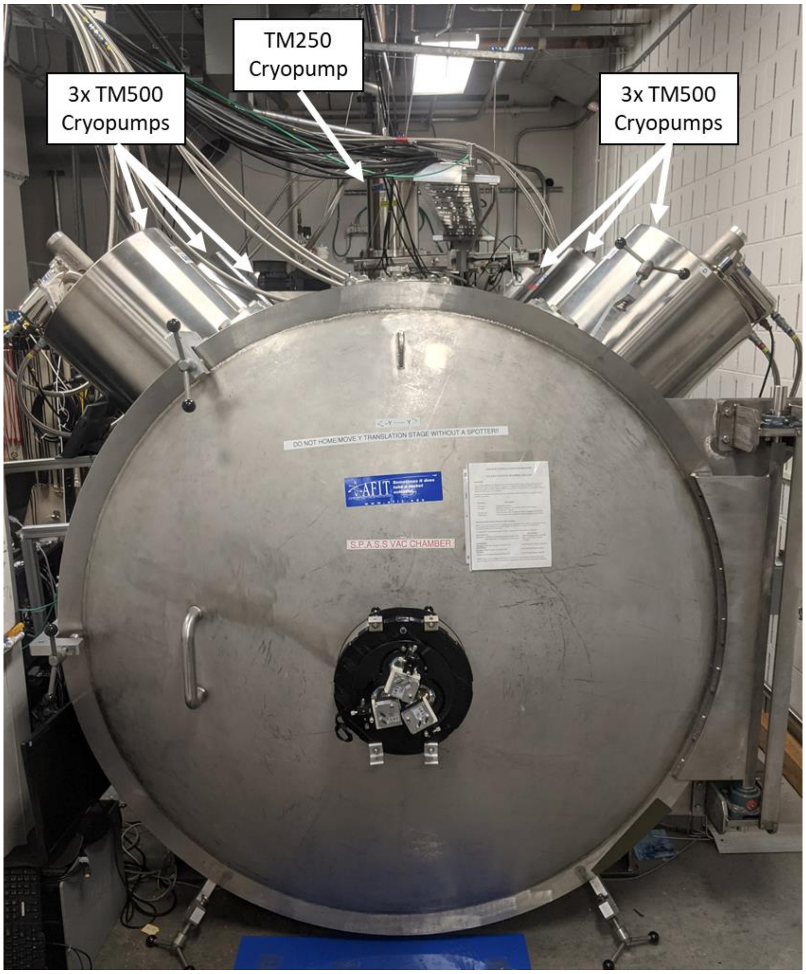

Figure 15. SPASS Vacuum Chamber

3.1.1 Vacuum Chamber Pumps

When beginning the pumping down of the SPASS chamber, an Oerlikon Leyhold SP250 roughing pump is first used to reduce chamber pressures to around 70 millitorr before a control system automatically switches over to a series of cryopumps to get the chamber down to its final operating conditions. The SPASS chamber was recently upgraded from four to six CVI Torrmaster TM500 cryopumps operating on liquid helium. Two additional TM250 cryopumps are mounted to the top of the vacuum chamber. These cryopumps are attached to a chilled plate that remove energy from particles that come in contact with it, allowing for significantly lower pressures than just the roughing pump. With the two new cryopumps installed, the chamber can now achieve pressures down to 10^{-6} Torr.

Pressure within the chamber is monitored with a Extorr Residual Gas Analyzer (RGA) at low chamber pressures. The RGA performs sweeps on the gases contained within the chamber, and produces chamber pressures as well as outputs of the atoms that have been identified within the chamber sorted by atomic mass. Due to aliasing, elements of atomic numbers over 100 are identified at lower atomic mass numbers. The RGA is capable of measurements down to 10^{-11} Torr.

3.2 Dye laser

A new dye laser system was installed next to SPASS chamber to conduct these experiments on an air cushioned rack to reduce environmental disturbances. The entire system can be seen in Figure 16. Cobra Stretch dye laser configuration on air cushioned rack.

Pumping of the dye laser is achieved with a Quanta Ray LAB-190-10H Pulsed Nd-YAG laser outputting two laser beams at 532 nm and 381 nm. This system operates at repetition rates from 1 to 50 Hertz with energies in excess of 500 mJ/pulse [30]. A power supply with analog controller was installed with the pump laser, requiring installation a Neslab Thermoflex 3500 water chiller with a cooling capacity of 3500 Watts with recirculation temperatures ranging between 5 and 90° C. The chiller was capable of keeping recirculated water at the desired 10°C during laser operation for both the pump laser and its power supply simultaneously. The pump laser was also connected to the lab’s nitrogen supply to nitrogen purge the system. The entire shelf was enclosed with plexiglass to prevent alignment issues with the pump and dye lasers. Additional shielding was installed between the pump and dye laser to prevent any scattered light from leaving the exposed area between the pump and dye lasers where alignment mirrors are placed.

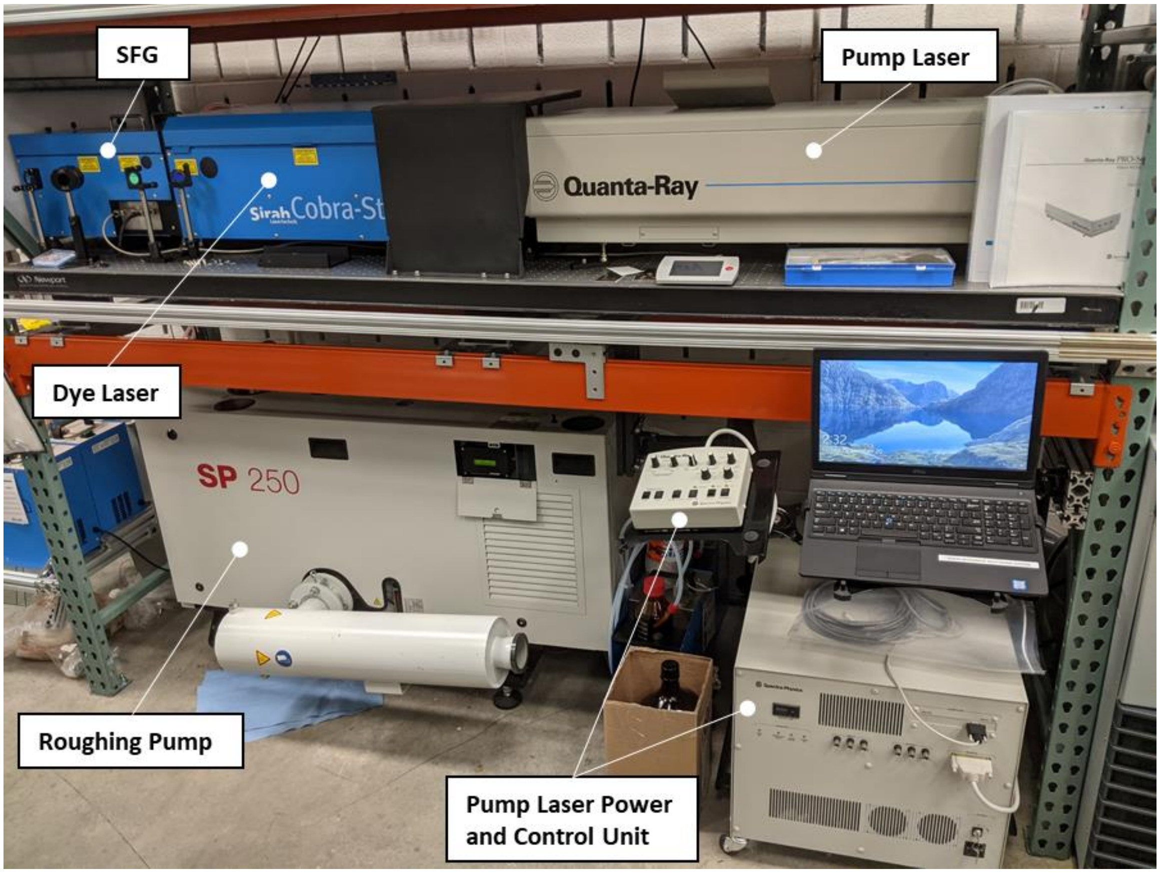

Figure 16. Cobra Stretch dye laser configuration on air cushioned rack

The output beams from the pump laser then were directed into a Sirah Cobra Stretch dye laser operating with a DCM special dye at a concentration of .1 g/L of ethanol. The 532 nm beam is run through the optical layout and through two dye cells, while the 381 nm beam passes through and is used for frequency mixing. Two dye pumps cycle the dye mixture through the two laser dye cells of 20 mm and 40 mm in length. Dye use is logged to ensure that the dye is at operation levels before laser firing and the pump should be run for 30 minutes per week when not in use to prevent buildup in the lines and tanks. DCM has a broad tuning range between 602 to 660 nm and has high efficiencies of ~30% in this range when compared to other dyes [21] and can be run for 500 Wh before needing replacement [31]. DCM special is a modified compound tuned to reach maximum efficiencies in the 590 nm range.

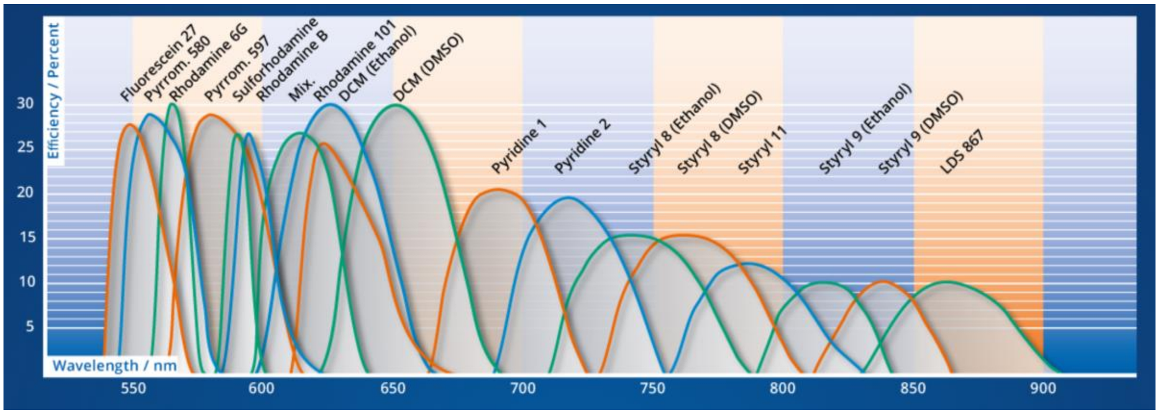

Figure 17. Various dye efficiencies for the Cobra Stretch dye laser [21]

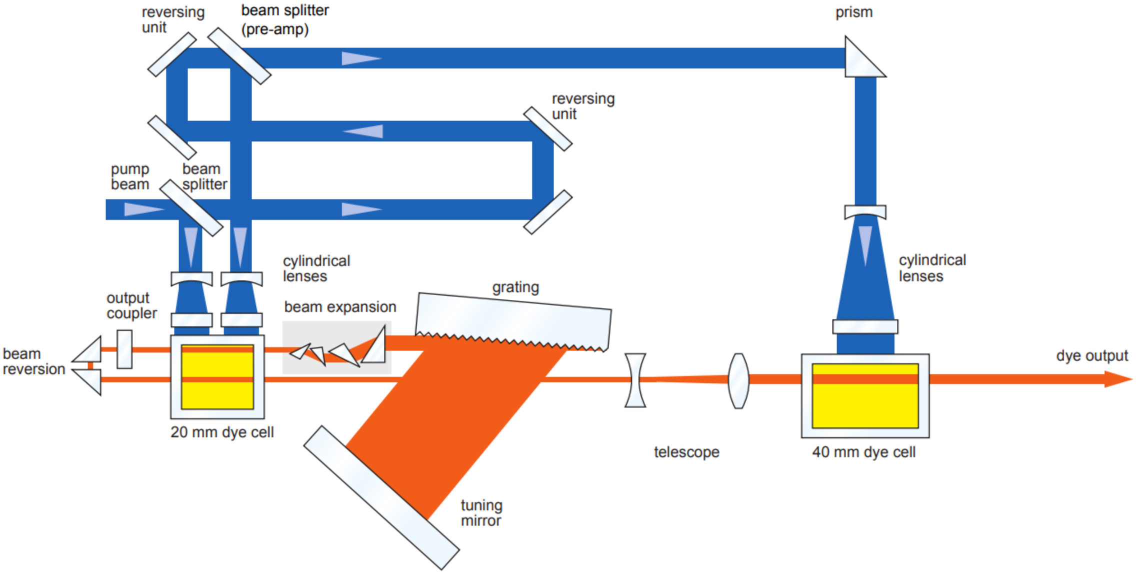

Figure 18. Cobra Stretch dye laser optical layout [18]

To get down to the desired operating wavelength of 222 nm for the laser, a Sirah frequency conversion system was installed directly at the exit of the dye laser and uses SFG to achieve the desired wavelength. After SFG, the dye laser produces a 222 nm laser beam at around 15 mJ/pulse (or 1.67×10^{16} photons/pulse), 5 millimeter beam diameter, pulse width of about 8 ns, and a repetition rate of 10 Hz [21] [30]. A laptop preloaded with software is used to control and tune the dye laser and frequency conversion system to the desired frequency or sweep a small range of frequencies.

The 222 nm laser beam path into the SPASS chamber was enclosed for safety with a combination of steel conduit and 3-D printed ULTEM parts. Support structure was built using 80/20 aluminum beams and wall mounts. S and P polarized mirrors designed for reflecting ultra-violet light on adjustable mounts were fixed the enclose corners.

Figure 19. 222 nm Laser Beam Enclosure

The beam entered the SPASS chamber through a vacuum safe 6 inch diameter, ¼ inch thick DUV quartz glass window from Lesker that has ultra-violet transmission of greater than 99.8% [32].

Once the beam has been brought into the chamber, another series of mirrors are required to bring the laser into the thruster plume. A lens is then required to focus the laser beam down to small area where the photon density is sufficient to achieve the REMPI process. The plasma region generated by the REMPI process due to a high powered laser can be approximated as a prolated ellipsoid. In similar experimentation looking at REMPI in xenon with a 224.3 nm dye laser, the ellipsoid was estimated to have a semimajor axis of 2 mm, a semiminor axis of 0.05 mm, and eccentricity of .9997 [28]. This equates to a testing volume of around 0.021 mm^3. The semiminor axis corresponds to the radius of the focused laser beam to achieve REMPI, so a radius of 0.05 mm leads to a required focus beam area of 0.007854 mm^2. Knowing the beam width and focal length of the lens used, the ionization region can be identified.

3.3 Microwave Scattering System

The microwave scattering systems used was designed by Spectral Energies, and utilizes a single microwave horn as a transceiver in the 8-12 GHz region of the microwave spectrum. The system is capable of determining number density and velocity of neutral xenon atoms depending on the experimental setup. The system contains a Keysight ESA Network Analyzer capable of producing microwave radiation between 100 kHz and 14 GHz, a Homodyne microwave scattering system box designed by Spectral Energies, a L3Harris Narda-ATM microwave horn with a nominal gain of 15 dB, and an oscilloscope for data collection. The polarization of the microwave radiation coming from the horn needs to be aligned with the propagation direction of the laser beam to maximize the scattering signal [28].

3.3.1 Number Density Measurements

The microwave horn is placed inside of the vacuum chamber and aligned such that the ionization region is placed in the center of the gain pattern and the distance from the horn set to for all experiments to ensure accurate measurements. The horn was connected to a pass-through in the chamber and connected to the microwave source. A continuous microwave source is required and is achieved by setting the start and stop frequencies to the same value in the Network analyzer. A photodiode is placed facing the laser beam as it enters the chamber to allow for a control measurement and normalization of the signal (Figure 20. Number density microwave scattering system diagram).

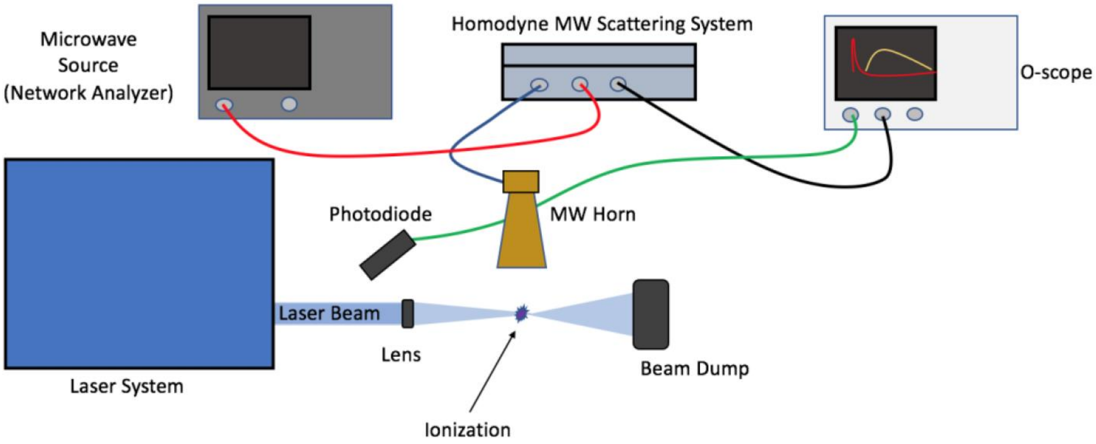

Figure 20. Number density microwave scattering system diagram [33]

During the experiment, a sweep of the microwave frequencies is done to identify the resonance frequency associated with the REMPI scheme desired. When looking for the electrons freed from neutral xenon via 2+1 REMPI, this frequency should be located at the resonance frequency where the strongest signal is received [33]. By performing the experiment on some vessels containing known densities of xenon, a linear scaling of scattered signal versus number density can identified. With this calibration, the experiment can be conducted on the Hall thruster plume to find the number densities. Since the scattering system measures free electrons, ions generated by the REMPI process will be measured, as the high speed ions accelerated by the thruster have not freed electrons outside of the thruster channel. High speed ions may be excited or further ionized by the high intensity of photons, but the resonance measured will only measure the electrons freed from the ground to first ionization state.

The laser system will produce 10 pulses per second allowing for a measurement at each pulse. To ensure accurate measurements of the mean and standard deviation of the signal, multiple pulses (minimum of 3, and thus 30 measurements) are required. A nominal value of 10 pulses producing 100 measurements is a desired minimum. The data is collected and stored on the oscilloscope for processing.

3.3.2 Velocity Measurements

For velocity measurements of neutral xenon, the microwave horn will be placed at an angle of incidence to the thruster to allow for the doppler measurement as seen in Figure 21. Velocity measurements of neutral xenon.

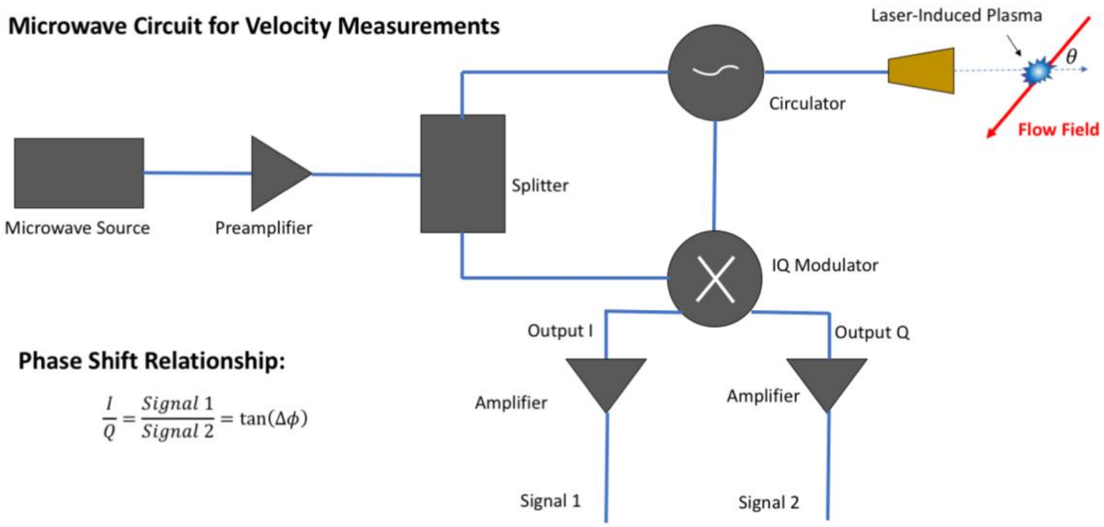

Figure 21. Velocity measurements of neutral xenon [33]

As discussed earlier, the received signal will be shifted with respect to the transmitted signal allowing for velocity measurements from the Doppler effect. Again, data from the microwave scattering system can be viewed on an oscilloscope, and saved into a comma separated value format for data processing. The REMPI process does slightly alter the velocity of atoms as photons do have momentum [34], this is further explored in Section 4.

The ultimate goal of this system is to be able to measure the velocities of atoms returning into the thruster, providing more thrust than would be achieved on orbit. To determine this, the velocity of neutrals as they exit the thruster just propelled by the back pressure of the xenon lines will be measured. The measurement of the shifted return signal will give the integrated velocity over the test volume. Once the unpropelled atoms are measured, testing can commence while the thruster is powered on. If neutral atoms are traveling back towards the thruster plane and pass through the ionization region, less of a Doppler shift should be seen in the scattering measurements when compared to the powered off tests.

3.4 Thruster Traverse

To determine the distribution of neutral xenon in the Hall thruster plume, the thruster must be moved to allow for different sections of the plume to be measured. The SPASS chamber contains a traverse system to allow for translation in three directions. To measure the entire plume, the thruster will need to be maneuvered in the Y and Z directions with respect to the coordinate system shown in Figure 22. Thruster Traverse.

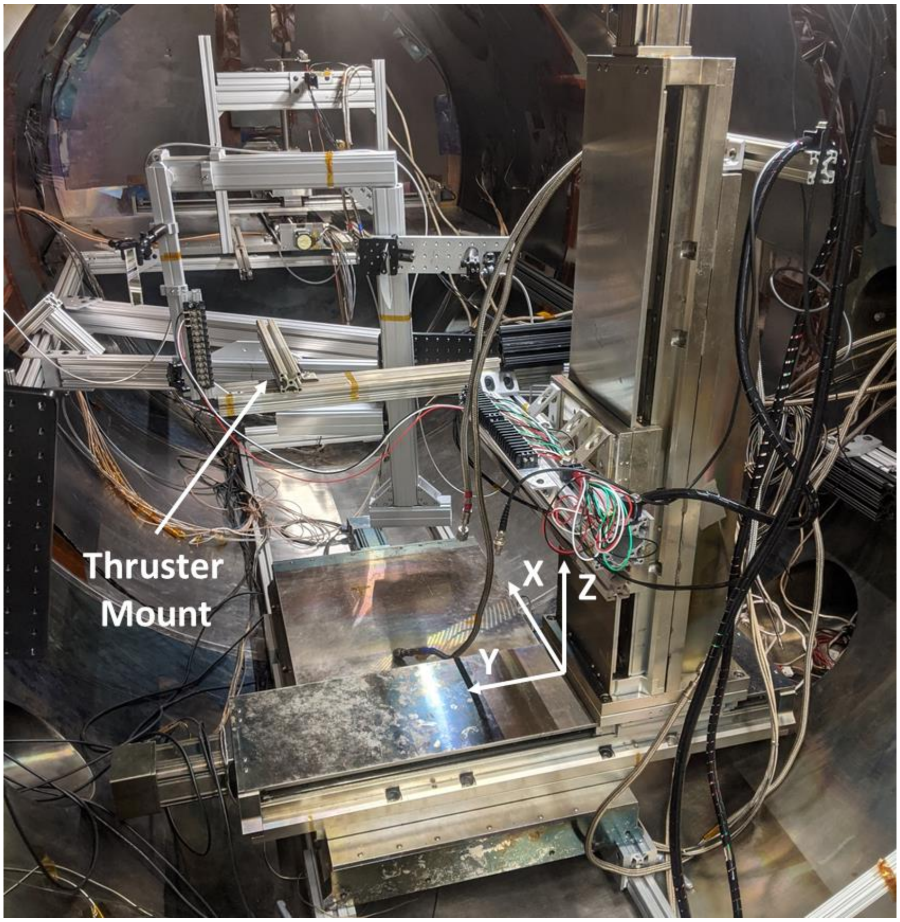

Figure 22. Thruster Traverse

3.5 Test Conditions

The microwave scattering system requires calibration before experimentation can be carried out on the Hall thruster. Vessels containing known densities of xenon are needed, allowing for a relationship between laser intensity and the scattering signal that should be nearly linear [28]. With this relationship found via calibration, the number density of neutral xenon can be extrapolated from the scattered signal during Hall thruster experiments.

The first testing condition will be to verify that the microwave scattering system can accurately measure the number density of neutral xenon with the thruster not being powered and flow only coming from the injectors. These atoms should be traveling at speeds near the thermal velocity of xenon at 138 meters per second [35]. This condition can be done either in vacuum or at atmospheric pressures. This measurement will be made in a small volume defined by the ionization region ellipsoid, with the thruster moved in the Y and Z directions via the traverse to get measurements in the entire plume at a certain distance from the thruster exit plane. The flow controllers on the xenon tank provide an accurate measurement for the actual flow rates of xenon exiting the thruster allowing for comparison with the measurements from the scattered signal.

After the system has proven to accurately measure xenon number densities coming from just the injectors, the thruster will be powered on for the second testing condition. Due to the mass utilization results from Bui [5], the same method of measuring number densities should produce results showing about 20% of the initial mass flow from the xenon tank flow controller.

As the laser system was not ready for validation due to time constraints, a model calculating the number densities of various species during a high intensity laser pulse will be used to prove that the new laser system will perform as expected. The two testing scenarios will be holding the mass flow rate (and thus the number density of neutral xenon in the testing volume) constant and varying the laser intensity to evaluate how much ionization will occur. The second testing condition will be holding the laser intensity constant and varying mass flow rates.

IV. Analysis and Results

The verification of the radar REMPI system coupled with the microwave scattering system to detect number density and velocity profiles of a Hall thruster plume is still pending. Due to unforeseen circumstances and time constraints, the needed optical mounts required to direct the 222 nm beam into the SPASS chamber did not arrive in time for verification testing. Previous experimentation has proven that a similar measurement system was able to accurately measure number density of neutral xenon with vessels of varying densities of xenon [28] [36]. Modeling of expected results match closely the experimentally derived data to show that ionization model can be explored for this research. An analysis of these previous results was expanded to show what results may be expected when the system is fully operational in the SPASS chamber.

4.1 Modeled Number Density Measurement Projections

Using the model outlined in References [28] and [36], simulations were conducted to determine the percentage of ionization that can be expected from the laser system at various operating conditions using Simulink. Terms containing species that were not pertinent to this experiment were neglected. Simulations of the expected output from the microwave scattering system were also conducted. The model contains equations for the rate of change of electron density, xenon number density, excited xenon, and ionized xenon as a function of time. Equations 41 through 47 comprised of the ionization model.

$$\frac{dn_e}{dt} = n_{Xe^*}\sigma_{Pi}F - \beta_{eff}n_e n_{Xe^+} - \beta_{dis}n_e n_{Xe_2^+} \tag{41}$$

$$\frac{dn_{Xe^+}}{dt} = n_{Xe^*}\sigma_{Pi}F - \beta_{eff}n_e n_{Xe^+} - k_{convXe}n_{Xe^+}n_{Xe}^2 \tag{42}$$

$$\frac{dn_{Xe^*}}{dt} = n_{Xe}\sigma^{(2)}F^2 - n_{Xe^*}\sigma_{Pi}F \ - k_e n_e n_{Xe^*} \tag{43}$$

$$\frac{dn_{Xe_2^+}}{dt} = -k_{convXe}n_{Xe^+}n_{Xe}^2 \ - \beta_{dis}n_e n_{Xe_2^+} \tag{44}$$

$$\frac{dn_{Xe}}{dt} = -\frac{dn_{Xe^*}}{dt} - \frac{dn_{Xe^+}}{dt} - \frac{dn_{Xe_2^+}}{dt} \tag{45}$$

$$\beta_{eff} = -1.7x10^{-20}T_e^{-4.5} + 3.02x10^{-16}T_e^{-0.75}\ [m^3/s] \tag{46}$$

$$\beta_{dis} = 2.3x10^{-12}(300/T_e[K])^{0.6}n_e[m^3/s] \tag{47}$$

where n_{Xe^*} is the number density of excited xenon, n_{Xe}^{+} is the number density of xenon ions, $n_{Xe_2^+}$ is the number density of xenon atoms combined in a reaction of Xe^+ with two Xe atoms, n_e is the number density of electrons, F is the photon flux provided by the laser, β_{eff} is the effective recombination rate between electrons and xenon ions, β_{dis} is the dissociative recombination rate between electrons and xenon dimer ions. Constants in these equations were pulled from [36], and include the photon-ionization cross section σ_{Pi} was chosen to be $2.43x10^{-23}$ m^2, the normalized cross section $\sigma^{(2)}$ was chosen to be $4.9x10^{-42}$ m^2, the rate constant of $n_{Xe_2^+}$ is k_{convXe} was chosen as $3.6x10^{-43}$ m^6/s^{17}, and the quenching rate constant of the excited state by electrons k_e was chosen to be $6x10^{15}$ m^3/s.

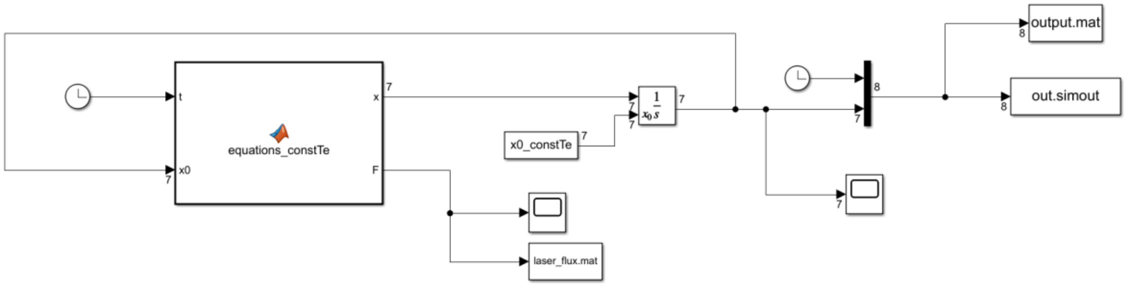

Figure 23. Simulink Model

To numerically integrate these equations, ODE15S was utilized within MATLAB as a Simulink model with a maximum step size of 1e-12. Joule heating was neglected in this model, and electron temperature was held constant; a suitable assumption in vacuum conditions. Laser pulse energy was simulated by a Gaussian distribution with a pulse width of 8 nanoseconds and a peak energy ranging from 5 to 50 mJ/pulse. This was then converted into the photon flux, F, used in the above differential equations. The peak energy of the laser was chosen to be at 35 nanoseconds to observe the behavior as the laser pulse begins. The length of the simulation was chosen to be 250 ns to observe the ion recombination with the freed electrons. Initial conditions for the model were $n_e(0) = n_{Xe*}(0) = n_{Xe^+}(0) = n_{Xe_2^+}(0) = 0$. The sampling location was chosen to be 40 centimeters from the thruster plane, and a divergence angle of 20° was chosen. The initial number density of xenon varied based on the testing conditions of the different model scenarios.

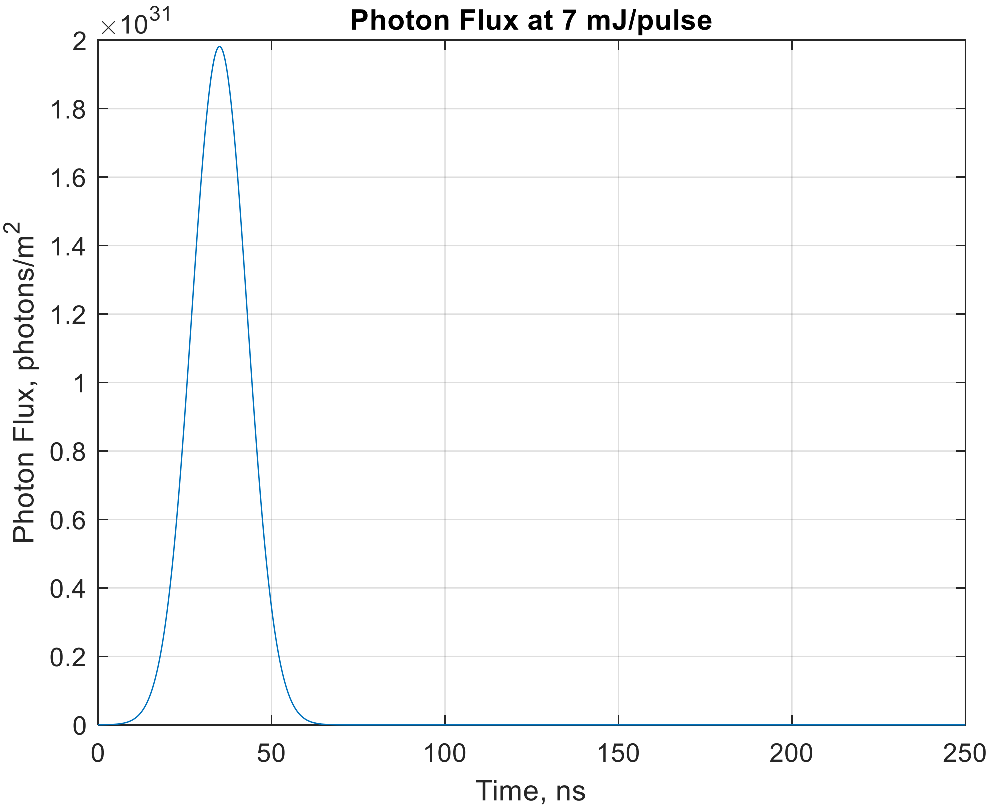

Figure 24. Laser pulse used in model

The model shows that as the pulse energy increases, a large amount of xenon is ionized very quickly. After the pulse has finished, the free electrons combine with the xenon ions to become neutral atoms again. It is interesting to note that the shape of the ionization curve is dependent on the mass flow rate of xenon and the pulse energy. At lower mass flow rates, the amount of xenon being ionized tends to remain nearly constant after the laser pulse reaches its peak energy, while at higher mass flow rates the number density of xenon ions begins decreases after the peak energy is achieved (Figure 25. Number densities of neutral xenon and ionized xenon for different mass flow rates).

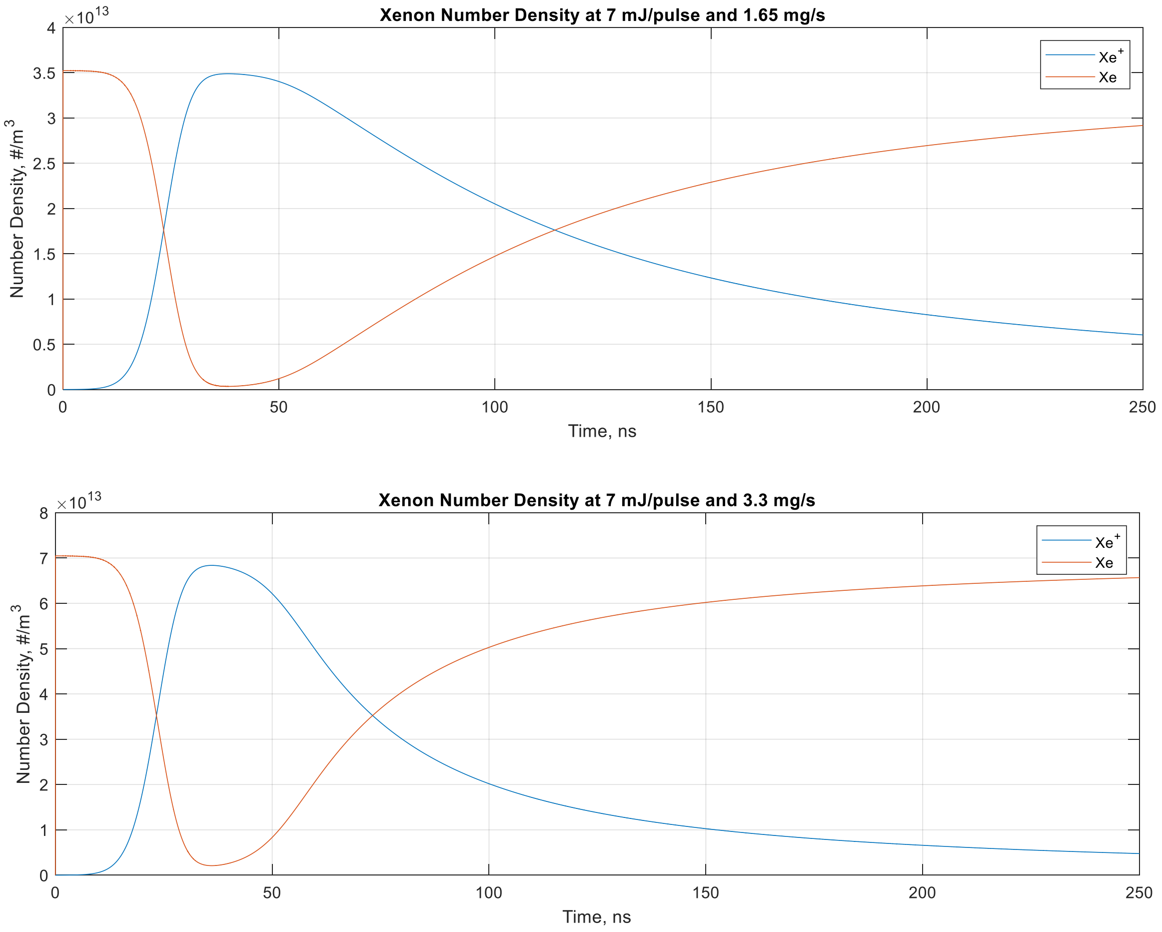

Figure 25. Number densities of neutral xenon and ionized xenon for different mass flow rates

The first condition tested in the model was with a constant mass flow rate of 3.3 mg/s flowing through the thruster without the thruster firing and pulse energies varying from 5 mJ to 50 mJ. As the laser energy increases, the percentage of xenon that has been ionized should increase, as there are more photons available per xenon atom to free an electron.

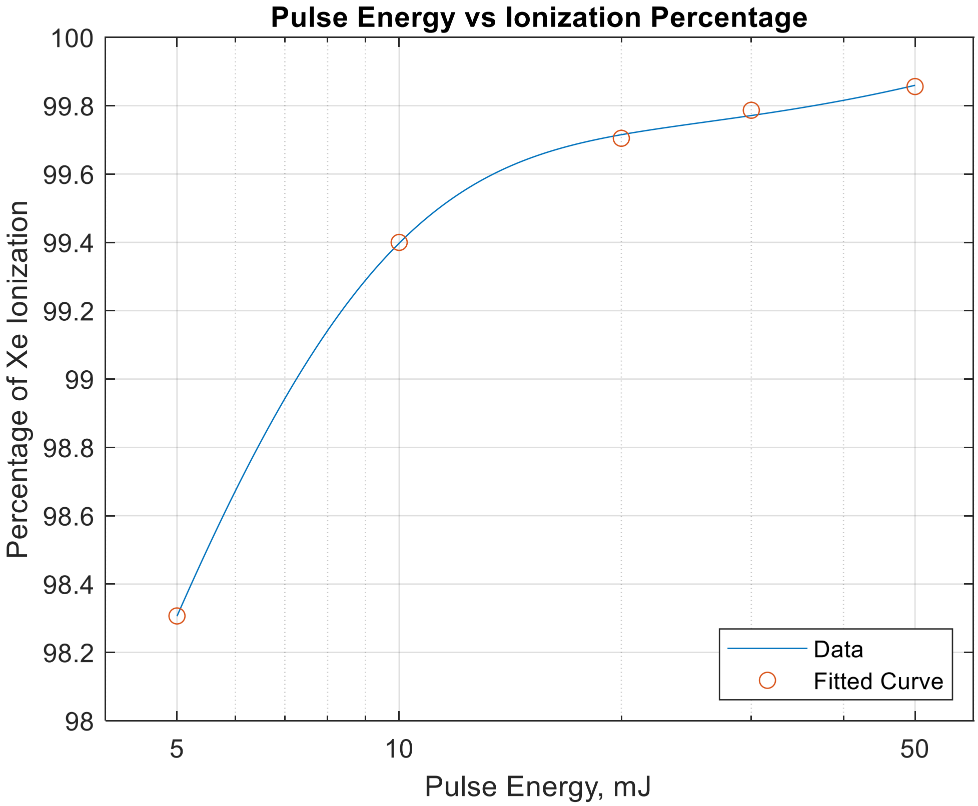

Figure 26. Ionization Percentage in first test of the model

As expected, as the pulse energy is increased a higher percentage of xenon is ionized. The data from the first test with the model is shown in Table 2. Ionization percentages from variable pulse energy model and was fit to an exponential that can be interpolated as needed to find the ionization percentage for a given peak laser energy for the given conditions:

$$Ionization\ \% \ = 99.64e^{4.405e-5*I_{peak}} - 6.424e^{-0.3111*I_{peak}} \quad (48)$$

Ionization Percentage	Pulse Energy (mJ)
98.31	5
99.40	10
99.70	20
99.79	30
99.86	50

Table 2. Ionization percentages from variable pulse energy model

The second condition tested with the model was a constant pulse energy of 7 mJ and mass flow rates ranging from 0.825 mg/s to 3.3 mg/s.

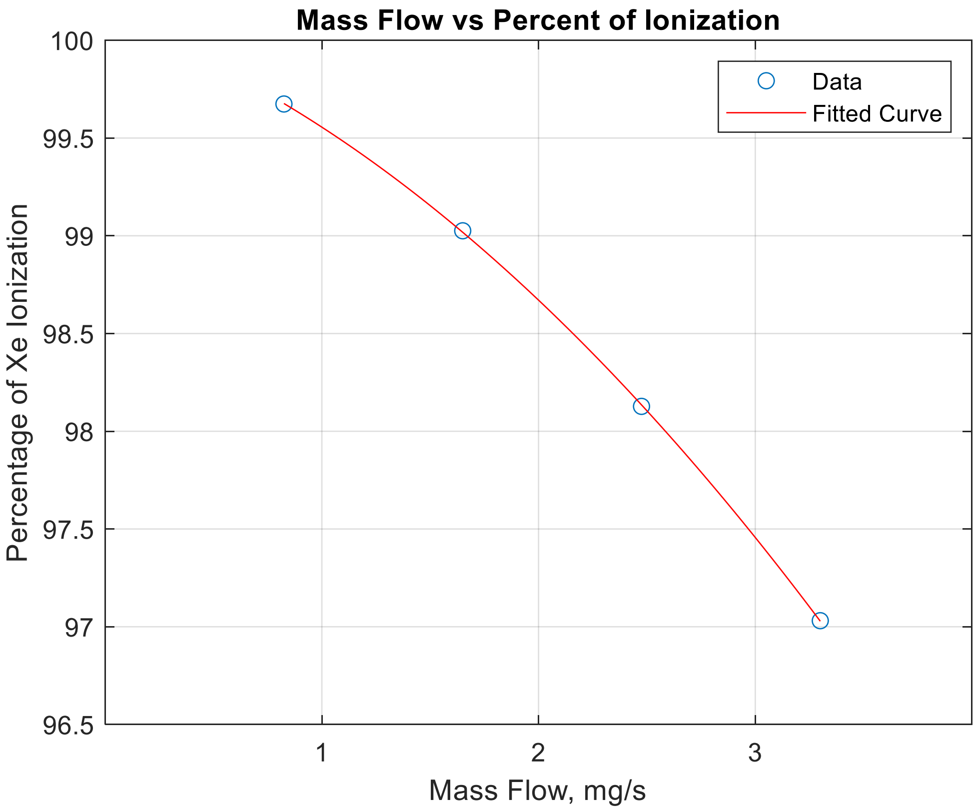

Figure 27. Ionization percentage in the second test of the model

From the model results it can be seen that at lower mass flow rates lead to higher ionization percentage that is to be expected as there would be more photons per xenon atom available for ionization. The data was fit to a polynomial that can be interpolated as needed to find the ionization for a given mass flow rate:

$$Ionization\,\% = -0.1645 * \dot{m}^2 - 0.3915 * \dot{m} + 100 \tag{49}$$

Ionization Percentage	Mass Flow Rate (mg/s)
99.67	0.825
99.03	1.650
98.13	2.475
97.03	3.300

Table 3. Ionization percentages from variable mass flow model

Ultimately the model shows that the installed laser system will be sufficient to ionize greater than 97% of the xenon in the test region. The model also does not account for the fast moving xenon atoms that will be traveling through the test volume when the Hall thruster is powered on. These atoms will absorb some of the laser photons, however there should be enough photons to ionize the slow moving neutrals also in the test section.

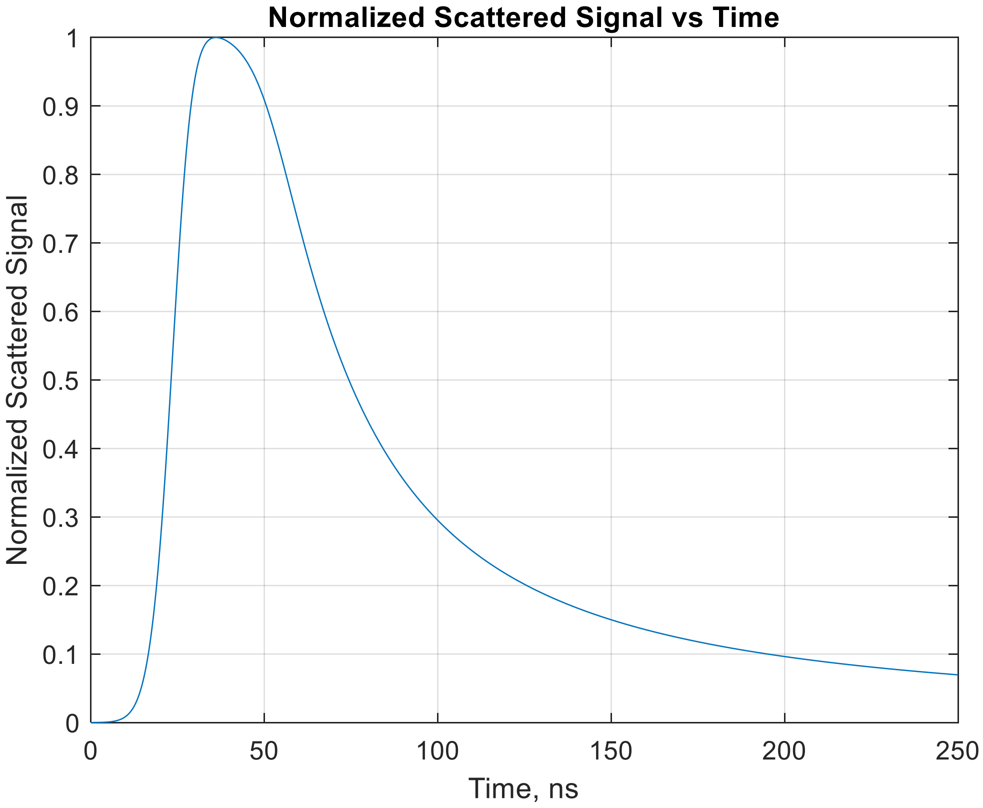

Figure 28. Estimated scattered signal from the model

Since the scattered microwave signal is proportional to the electron number density [28] [36], Figure 28. Estimated scattered signal from the model was generated to show what a returned microwave signal will look like to show the presence of free electrons in the test volume. Once the system is calibrated, the returned scattered for a test can interpolated from the calibrated results to determine the number density of xenon atoms in the test volume.

The results from the model show the xenon being immediately excited by the laser, and returning to the excited state after the ions have recombined with the electrons freed by the laser. This was likely due to the implementation of the model and should not have a large effect on the projections.

4.2 Velocity Profile Projections

The bombardment of high energy photons may change the velocity vector of neutral xenon when measured with the microwave scattering system. Experimentation has shown that this recoil velocity can indeed change the velocity vector of impacted particles, however slightly [34]. Current theories suggest that the rest mass of a photon in free space is zero and that a photon also has non-zero rest mass that is wavelength-dependent [37]. The momentum is known is of a photon as a function of wavelength, given by [38]:

$$\vec{p}_{photon} = \frac{h}{\lambda} \tag{50}$$

The momentum vector of a photon is along the direction of propagation.

Solving for the momentum of three photons at 222 nm gives a total momentum of $8.96\text{x}10^{-27}$ kg m/s. In the worst case scenario where the photons from the ultraviolet laser impact xenon atoms in the Hall thruster plume at 90° and thus maximize the change in velocity vector, the following analysis shows how much change in velocity can be expected.

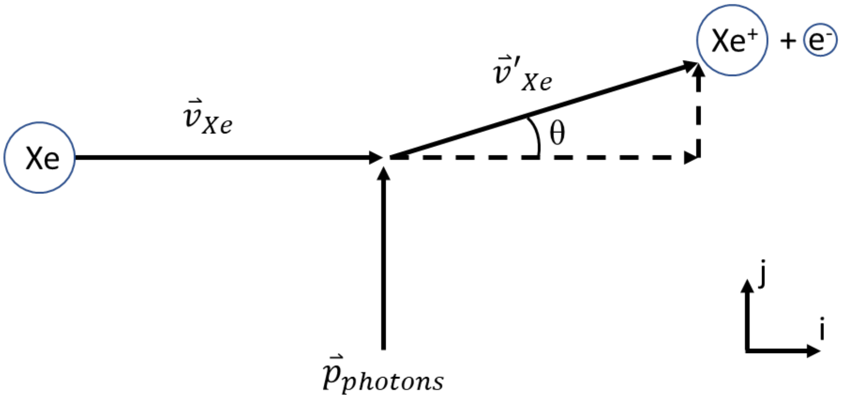

Figure 29. Change in velocity vector after photon bombardment

Assuming that the unaccelerated neutral xenon atoms are traveling in the i direction (see Figure 29. Change in velocity vector after photon bombardment), a velocity component in the j direction after collision can be found with:

$$\vec{v}'_{Xe,j} = \frac{3 \cdot \vec{p}_{proton}}{m_{Xe}} \tag{42}$$

Using Equation 42, the added component to the xenon velocity vector was found to be 0.041 m/s. When looking for the angle between the before and after collision velocity vectors, the angle can be found with:

$$\theta = \tan^{-1}\frac{0.041}{v_{Xe}} \tag{51}$$

Assuming xenon is traveling at its thermal velocity of 138 m/s at room temperature, this would correspond to a 0.017° change in the velocity vector. While not a significant change occurs due to this recoil velocity, this phenomenon may be observable and may need to be taken into account. Additionally, depending on the geometry of the interaction, spin may be imparted onto the xenon atom.

The change in mass of the xenon atom as a result of losing an electron was not considered in this analysis as the mass of xenon is much greater than the mass of an electron, as was the direction of the ejected electron. Depending on the geometry of the photon-xenon collision, the ejected electron could be ejected at slightly different angles depending on the location in the electron cloud as shown in Figure 30. Possible electron ejection vectors. Again, the spin of the electron was neglected

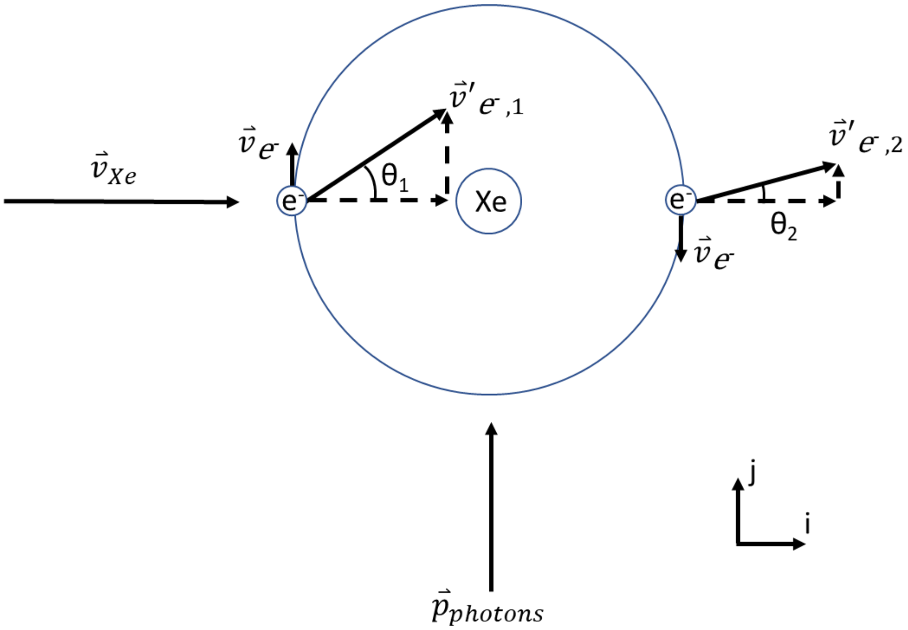

Figure 30. Possible electron ejection vectors

V. Conclusions and Recommendations

The performed analysis shows that the dye laser system installed at the SPASS lab will be sufficient to ionize xenon in the BHT-600 Hall thruster plume to perform microwave scattering measurements on the free electrons. Through a range of laser intensities and mass flow rates ionization percentages of greater than 97% should be achievable. Previous experiments have shown that microwave scattering can provide velocity profiles of ionized atoms, and the photon bombardment should not heavily impact the velocity vectors of the studied atoms.

5.1 Significance of Research

Observation of neutral atoms allows for unobtrusively obtained full characterization of Hall thruster plumes when combined with other methods mentioned. Previous work has focused on the high velocity xenon ions accelerated by the thruster, but a method of measuring neutrals allows for a better understanding of anode injection distribution and may allow for measurement of neutrals returning to the thruster after interaction with the chamber walls. The installed laser with microwave scattering measurement system should allow for high resolution measurements that allow insight into unanswered questions regarding Hall thruster plumes.

5.2 Recommendations for Future Research

Calibrated volumes of xenon will be required to develop the relationship between a scattered signal for this system and the number density of xenon before measurements in the plume can occur. This relationship is system dependent and is a function of microwave frequency, horn-testing region displacement/location and the species being studied. Care should be taken to make sure the testing region is located in the center of the antenna gain pattern. Previous experimentation has shown this relationship nearly linear, and once the calibration has been conducted number densities within the Hall thruster plume can be found by comparing the scattered signal to the calibrated relationship. The number density can be found by interpolation.

Due to the large cross sectional volume of the Hall thruster plume with respect to the ionization region studied, a large number of testing locations would be needed to obtain a full field measurement of the thruster. With an estimated thruster plume cross sectional volume of 7.783×10^{-5} m^3 and a testing volume of 2.1×10^{-11} m^3, an unrealistic roughly 3 million testing locations would be needed to full characterize the flow field. Assuming symmetrical dispersion, this number may be drastically reduced but will still require many testing locations to fully characterize the plume. Assumptions must be made in order to bring the number of testing locations to a reasonable number. In reality, around 300 testing locations would be more reasonable and allow for generalization to be made to estimate the full field distribution.

Previous experimentation done with microwave scattering to observe plasmas proved to be accurate but susceptible to scattering off background objects [39].

Microwave scattering systems are prone to noise from outside sources, it is recommended that some method of preventing the scattering of microwaves beyond the testing region. The chamber is stainless steel, and is ideal for scattering these microwaves so noise mitigation may be an important factor. The primary sources of noise are likely to come from reflections in the chamber due to side lobes of the transceiver horn or the main lobe as the antenna gain pattern will have an associated spreading angle that is much larger than the ionization region.

Once operational, the new dye laser coupled with the microwave scattering system will ideally allow insight into three key areas where future work will be needed to address.

This new system will allow for studying is the distribution of neutral xenon coming out of the anode injectors. It has been assumed that the injectors provide a uniform distribution in the thruster chamber to allow for maximum ionization via the high speed circulating electrons, but this is likely not the case. By running the thruster with a known mass flow rate of xenon and no discharge current applied, the distribution coming from the injectors can be analyzed.

Precise mass utilization calculations should also be achievable with this new system. As the scattering system is tuned to only detect neutral xenon, precise number densities can be directly measured as opposed to measuring xenon in different ionization states and using this data to infer the mass utilization.

The final area where this new system can provide much needed insight is to determine how much xenon returns into the thruster chamber due to the finite volume chamber, producing extra thrust. This information can be found by looking at the plasma velocity measurements as the vacuum chamber is pumped down to its lowest pressures. With the thruster powered on and fired as the chamber is pumped down, a correlation should be seen where the integrated velocity of the ionization region increases as chamber pressure decreases. As xenon is traveling back towards the thruster, the integrated velocity will be lower. Number density measurements combined with the velocity measurements should allow for a determination of how much xenon is reentering the thruster, with the ultimate goal of using this information to estimate how much extra thrust is being produced when compared to on-orbit operation.

Appendix

MATLAB Files and Functions Used

sim_init.m

```
% Initialization Script for Simulink Model
% Taylor Foy
% AFIT/ENY

clear all; close all; clc;

%% Simulation Parameters
dist = .4; % distance from thruster exit plane, m
theta = 20; % divergence angle, degrees
disk_area = pi*(.635+dist*tand(theta))^2-pi*(.483-dist*tand(theta))^2; % area
of disk m^2
disk_depth = .05/1000; % diameter of ionization region m
disk_vol = disk_area*disk_depth; % total volume at dist, m^3
v_th = 138; % thermal velocity of xe, m/s
mdot_percent = 1;
mdot = mdot_percent*3.3/1000^2; % mass flow rate, kg/s
time_disk = disk_depth/v_th; % s
kg_in_disk = mdot*time_disk; % mass of xenon in disk, kg
disk_density = kg_in_disk/disk_vol; % density of xenon in disk, kg/m^3
num_density = (6.02214076e23/131.293)*disk_density; % # density of xenon in
disk, #/m^3

e = 1.60217662e-19; % electron charge, C
k = 1.380649e-23; % boltzman's const
Te = 300*k/e; % electron temperature, eV

%% Defining initial conditions and states
% ne =         x0(1);
% n_Xe =       x0(2);
% n_Xe_star =  x0(3);
% n_Xe_i =     x0(4);
% n_Xe_2i =    x0(5);
% beta_eff =   x0(6);
% beta_dis =   x0(7);

x0_constTe = [0 num_density 0 0 0 3.02e-16*Te^-.75 0];

tf = 250e-9; % Length of simulation (s)
```

Simulink User Defined Function to Solve Model Equations

```
function [x, F] = equations_constTe(t, x0) %, n_Xe_init)
% Simulink function to solve a system of couple differential equations
% Taylor Foy
% AFIT/ENY

%% Defining states from input
ne =         x0(1);
n_Xe =       x0(2);
n_Xe_star = x0(3);
n_Xe_i =    x0(4);
n_Xe_2i =   x0(5);
beta_eff =  x0(6);
beta_dis =  x0(7);

% Defining needed constants and parameters
c = 2.998e8; % speed of light, m/s
lam = 222e-9; % laser wavelength, m
h = 6.62607004e-34; % planck's const, m^2*kg/s
w_l = 2*pi*c/lam; % laser angular frequency, rad/s
sig_pi = 2.43e-23; % m^2
t_peak = 35e-9; % slight pulse delay, s
sig_pulse = 8e-9; % pulse length, s
sig_2 = 4.2e-43; % m^4*s
I0 = (.007/sig_pulse)/7.854e-9; % peak laser intensity, W/m^2
I = I0.*exp(-(t-t_peak).^2/(2.*sig_pulse.^2)); % laser profile, W/m^2
F = I./(h.*w_l); % photon flux, photon/m^2
e = 1.60217662e-19; % electron charge, C
k = 1.380649e-23; % boltzman's const
kconvXe = 3.6e-43; % m^6*s^-27
ke = 6e-15; % m^3/s
Te = 300*k/e; % electron temperature, eV

%% Rate Equations
% Eq 7
dnedt = n_Xe_star*sig_pi*F - beta_eff*ne*n_Xe_i - beta_dis*ne*n_Xe_2i;

% Eq 8
dn_Xe_idt = n_Xe_star*sig_pi*F - beta_eff*ne*n_Xe_i - kconvXe*n_Xe_i*n_Xe^2;

% Eq 9
dn_Xe_stardt = n_Xe*sig_2*F^2 - n_Xe_star*sig_pi*F - ke*ne*n_Xe_star;

% Eq 10
dn_Xe_2idt = kconvXe*n_Xe_i*n_Xe^2 - beta_dis*ne*n_Xe_2i;

dn_Xedt = -dn_Xe_stardt - dn_Xe_idt - dn_Xe_2idt;

% Eq 13
beta_eff = 1.7e-20*ne*Te^-4.5 + 3.02e-16*Te^-.75;

% Eq 14
beta_dis = 2.3e-12*ne*(300/(Te*(e/k)))^.6;
x = [dnedt; dn_Xedt; dn_Xe_stardt; dn_Xe_idt; dn_Xe_2idt; beta_eff; beta_dis;];
```

processing,m

```
% Processing Script for Simulink Model
% Taylor Foy
% AFIT/ENY

clc; clear all; close all;

%% Fixed Mass Flow, Variable Laser Intensity
% Loading constant mdot data files

mj5 = load('5mj_fullmdot.mat');
mj5_time = mj5.ans.data(:,1);
mj5_ne = mj5.ans.data(:,2);
mj5_nXe = mj5.ans.data(:,3);
mj5_nXe_star = mj5.ans.data(:,4);
mj5_nXe_i = mj5.ans.data(:,5);
mj5_nXe_2i = mj5.ans.data(:,6);

mj10 = load('10mj_fullmdot.mat');
mj10_time = mj10.ans.data(:,1);
mj10_ne = mj10.ans.data(:,2);
mj10_nXe = mj10.ans.data(:,3);
mj10_nXe_star = mj10.ans.data(:,4);
mj10_nXe_i = mj10.ans.data(:,5);
mj10_nXe_2i = mj10.ans.data(:,6);

mj20 = load('20mj_fullmdot.mat');
mj20_time = mj20.ans.data(:,1);
mj20_ne = mj20.ans.data(:,2);
mj20_nXe = mj20.ans.data(:,3);
mj20_nXe_star = mj20.ans.data(:,4);
mj20_nXe_i = mj20.ans.data(:,5);
mj20_nXe_2i = mj20.ans.data(:,6);

mj30 = load('30mj_fullmdot.mat');
mj30_time = mj30.ans.data(:,1);
mj30_ne = mj30.ans.data(:,2);
mj30_nXe = mj30.ans.data(:,3);
mj30_nXe_star = mj30.ans.data(:,4);
mj30_nXe_i = mj30.ans.data(:,5);
mj30_nXe_2i = mj30.ans.data(:,6);

mj50 = load('50mj_fullmdot.mat');
mj50_time = mj50.ans.data(:,1);
mj50_ne = mj50.ans.data(:,2);
mj50_nXe = mj50.ans.data(:,3);
mj50_nXe_star = mj50.ans.data(:,4);
mj50_nXe_i = mj50.ans.data(:,5);
mj50_nXe_2i = mj50.ans.data(:,6);

% Calculating ionization percentages
mj5_percent = max(mj5_nXe_i)/mj5_nXe(1);
mj10_percent = max(mj10_nXe_i)/mj10_nXe(1);
mj20_percent = max(mj20_nXe_i)/mj20_nXe(1);
mj30_percent = max(mj30_nXe_i)/mj30_nXe(1);
mj50_percent = max(mj50_nXe_i)/mj50_nXe(1);

fullmdot_y = [mj5_percent mj10_percent mj20_percent mj30_percent
mj50_percent]*100;
fullmdot_x = [5 10 20 30 50]';
```

```
f1 = fit(fullmdot_x, fullmdot_y', 'exp2')
x = linspace(5,50,1000);
f1 = 99.64*exp(4.405e-5*x)-6.424*exp(-.3111*x);

figure
semilogx(x, f1, fullmdot_x, fullmdot_y, 'o')
title('Pulse Energy vs Ionization Percentage')
xlabel('Pulse Energy, mJ')
ylabel('Percentage of Xe Ionization')
legend('Data','Fitted Curve', 'Location', 'southeast')
% xlim([0 55])
% ylim([98 100])
axis([4 60 98 100])
xticks([5 10 50])
xticklabels({'5', '10', '50'})
grid on

%% Fixed Intensity, Variable Mass Flow
% Loading files for Laser Intensity = 7 mJ/pulse

mj7_100 = load('7mj_100mdot.mat');
mj7_100_time = mj7_100.ans.data(:,1);
mj7_100_ne = mj7_100.ans.data(:,2);
mj7_100_nXe = mj7_100.ans.data(:,3);
mj7_100_nXe_star = mj7_100.ans.data(:,4);
mj7_100_nXe_i = mj7_100.ans.data(:,5);
mj7_100_nXe_2i = mj7_100.ans.data(:,6);
mj7_100_vm = mj7_100.ans.data(:,7);

mj7_75 = load('7mj_75mdot.mat');
mj7_75_time = mj7_75.ans.data(:,1);
mj7_75_ne = mj7_75.ans.data(:,2);
mj7_75_nXe = mj7_75.ans.data(:,3);
mj7_75_nXe_star = mj7_75.ans.data(:,4);
mj7_75_nXe_i = mj7_75.ans.data(:,5);
mj7_75_nXe_2i = mj7_75.ans.data(:,6);

mj7_50 = load('7mj_50mdot.mat');
mj7_50_time = mj7_50.ans.data(:,1);
mj7_50_ne = mj7_50.ans.data(:,2);
mj7_50_nXe = mj7_50.ans.data(:,3);
mj7_50_nXe_star = mj7_50.ans.data(:,4);
mj7_50_nXe_i = mj7_50.ans.data(:,5);
mj7_50_nXe_2i = mj7_50.ans.data(:,6);

mj7_25 = load('7mj_25mdot.mat');
mj7_25_time = mj7_25.ans.data(:,1);
mj7_25_ne = mj7_25.ans.data(:,2);
mj7_25_nXe = mj7_25.ans.data(:,3);
mj7_25_nXe_star = mj7_25.ans.data(:,4);
mj7_25_nXe_i = mj7_25.ans.data(:,5);
mj7_25_nXe_2i = mj7_25.ans.data(:,6);

% Calculating Ionization percentages
mj7_100_percent = max(mj7_100_nXe_i)/mj7_100_nXe(1);
mj7_75_percent = max(mj7_75_nXe_i)/mj7_75_nXe(1);
mj7_50_percent = max(mj7_50_nXe_i)/mj7_50_nXe(1);
mj7_25_percent = max(mj7_25_nXe_i)/mj7_25_nXe(1);
```

```
variable_mdot_y = [mj7_25_percent mj7_50_percent mj7_75_percent
mj7_100_percent]*100;
variable_mdot_x = [3.3*.25 3.3*.5 3.3*.75 3.3]';


f2 = fit(variable_mdot_x, variable_mdot_y', 'poly2')

figure
plot(f2, variable_mdot_x, variable_mdot_y, 'o')
title('Mass Flow vs Percent of Ionization')
xlabel('Mass Flow, mg/s')
ylabel('Percentage of Xe Ionization')
legend('Data','Fitted Curve')
xlim([0 4])
ylim([96.5 100])
xticks([1 2 3])
xticklabels({'1', '2', '3'})
grid on

%% Various other plots
laser_pulse_file = load('7mjlaser_flux.mat');
laser_pulse = laser_pulse_file.ans.data(:,1);

figure
plot(mj7_100_time(1:30:end)*1e9, mj7_100_ne(1:30:end)/max(mj7_100_ne))
xlabel('Time, ns')
ylabel('Normalized Scattered Signal')
title('Normalized Scattered Signal vs Time')
grid on

figure
plot(mj7_100_time*1e9, mj7_100_nXe_i, mj7_100_time*1e9, mj7_100_nXe_star)
xlabel('Time, ns')
ylabel('Number Density, #/m^3')
title('Xenon Number Density at 7 mJ/pulse and 3.3 mg/s')
legend('Xe^+', 'Xe')
grid on

figure
plot(mj7_50_time*1e9, mj7_50_nXe_i, mj7_50_time*1e9, mj7_50_nXe_star)
xlabel('Time, ns')
ylabel('Number Density, #/m^3')
title('Xenon Number Density at 7 mJ/pulse and 1.65 mg/s')
legend('Xe^+', 'Xe')
grid on

figure
plot(mj7_100_time*1e9, mj7_100_nXe_i/max(mj7_100_nXe_i), mj7_100_time*1e9,
mj7_100_nXe_star/max(mj7_100_nXe_star), mj7_50_time*1e9,
mj7_50_nXe_i/max(mj7_50_nXe_i), mj7_50_time*1e9,
mj7_50_nXe_star/max(mj7_50_nXe_star))
xline(35 , '--r')
xlabel('Time, ns')
ylabel('Normalized Number Density, #/m^3')
title('Xenon Number Density at 7 mJ/pulse, 1.65 and 3.3 mg/s')
legend('Xe^+ 100%', 'Xe 100%', 'Xe^+ 50%', 'Xe 50%', 'Location', 'east')
grid on

figure
plot(mj7_50_time*1e9, mj7_50_nXe_i, mj7_50_time*1e9, mj7_50_nXe_star)
xlabel('Time, ns')
```

```
ylabel('Number Density, #/m^3')
title('Xenon Number Density at 7 mJ/pulse and 1.65 mg/s')
legend('Xe^+', 'Xe')
grid on

figure
plot(mj7_100_time*1e9, laser_pulse)
xlabel('Time, ns')
ylabel('Photon Flux, photons/m^2')
title('Photon Flux at 7 mJ/pulse')
grid on
```

Bibliography

[1] D. M. Goebel and I. Katz, "Fundamentals of Electric Propulsion: Ion and Hall Thrusters," Jet Propulsion Laboratory, 2008.

[2] R. R. Hofer, P. Y. Peterson and A. D. Gallimore, "Characterizing Vacuum Backpressure Effects on the Performance of a Hall Thruster," Electric Rocket Propulsion Society, Ann Arbor, MI, 2001.

[3] G. Janes, J. Dotson and T. Wilson, "Momentum Transfer Through Magnetic Fields," in *Proceedings of Third Symposion on Advanced Propulsion Concepts*, Cincinnati, OH, 1962.

[4] V. Kim, "Electric Propulsion Activity in Russia," in *International Electric Propulsion Conference*, Pasadena, CA, 2001.

[5] D. M. Bui, "Characterization of Busek 600 W Hall Thruster," Air Force Institute of Technology, 2012.

[6] D. A. Kenan, "Xenon and Krypton Characterization in Satellite Thrusters," Air Force Institute of Technology, Wright Patteron Air Force Base, OH, 2010.

[7] J. T. Thurman, "Hall Thruster Plume Diagnostics Utilizing Microwave Interferometry," Air Force Institute of Technology, Wright Patterson Air Force Base, OH, 2008.

[8] A. Leonard, "Sheet Velocity Measurememnts Using Laser Absorbtion Spectroscopy in a Xenon Hall Effect Thruster," Air Force Institute of Technology, Wright Patterson Air Force Base, OH, 2019.

[9] R. B. Miles, M. N. Shneider, S. H. Zaidi and Z. Zhang, "Experiements on Microwave Scattering of REMPI in Argon, Xenon, and Nitric Oxide," Miami, FL, 2007.

[10] G. P. Sutton and O. Biblarz, Rocket Propulsion Elements, 9th ed., Hoboken: John Wiley & Sons, 2017.

[11] D. Jacobson and D. Manzella, "50 kW Class Krypton Hall Thruster Performance," in *39th AIAA/ASME/SAE/ASEE Joint Propulsion Conference and Exhibit*, Huntsville, AL, 2003.

[12] R. R. Hofer, "Development and Characterization of High-Efficiency, High-Specific Impulse Xenon Hall Thrusters," NASA, Ann Arbor, MI, 2004.

[13] H. Eichhown, K. H. Schoenbach and T. Tessnow, "Paschen's Law for a Hollow Cathode Discharge," Applied Physics Letters, Norfolk, VA, 1993.

[14] I. D. Boyd, C. Cai, M. L. R. Walker and A. D. Gallimore, "Computation of Neutral Gas Flow From a Hall Thruster Into a Vacuum Chamber," American Institute of Physics, Ann Arbor, MI, 2003.

[15] S. Mazouffre, D. Pagnon and J. Bonnet, "Two Ways to Evaluate the Xe+ Ion Flow in a Hall Effect Thruster: LIF Spectroscopy and Fabry–Perót Interferometry," AIAA, Fort Lauderdale, FL, 2004.

[16] K. e. a. Niemi, *Plasma Sources Science and Technology*, vol. 14, p. 375.

[17] P. W. Milonni and J. H. Eberly, Laser Physics, Hoboken, NJ: John Wiley & Sons Inc., 2010.

[18] Sirah Lasertechnik, *Cobra-Stretch Dye Laser Datasheet*, Edinburgh, 2018.

[19] ASE Optics, "Innovation," [Online]. Available: https://www.aseoptics.om/products-optronics/. [Accessed 10 6 2020].

[20] R. Boyd, Nonlinear Optics, Rochester, New York: Academic Press, 2008.

[21] Sirah Lasertechnik, "Sum Frequency Mixing with 355 nm," [Online]. Available: http://www.sirah.com/laser/frequency-conversion/mixing-with-355-nm. [Accessed 29 June 2020].

[22] A. Kramida, Y. Ralchenki, J. Reader and N. A. Team, "Spectra Database," National Institute of Standards and Technology, Gaithersburg, MD, 2019.

[23] J. H. Gross, Mass Spectroscopy: A Textbook, 3rd ed., Heidelberg, Germany: Springer, 2017.

[24] R. Hilborn, Einstein coefficients, cross sections, f values, dipole moments, and all that, Amhert, MA: Amherst College, 2002.

[25] V. Letokhov, Nonlinear Laser Chemistry, Berlin: Springer-Verlag, 1977.

[26] G. Ewing, "Microwave Absorption Spectroscopy," *Journal of Chemical Education,* vol. 43, 1966.

[27] R. Sorrentino and G. Bianchi, "Microwave and RF Engineering," John Wiley & Sons, West Sussex, United Kingdom, 2010.

[28] C. Galea, M. Shneider, T. L. Chng, A. Dogariu and R. Miles, "Radar REMPI Diagnostic for Low Neutral Density Measurements of Xenon in Helium Buffer Gas: Experiments and Modeling," in *AIAA 2018 Plasmadynamics and Lasers Conference*, Atlanta, 2018.

[29] L. D. Landau, L. P. Pitaevskii and E. Lifshitz, Course of Theoretical Physics Volume 8: Electrodynamics of Continuous Media, 2nd ed., Pergamon: Butterworth-Heinemann, 1984, p. Chap 1.

[30] Spectra-Physics, *Lab Series Pulsed Nd:YAG Datasheet,* Mountain View: Spectra-Physics, 2001.

[31] Sirah Lasertechnik, "DCM- Sirah Lasertechnik," Sirah Lasertechnik, [Online]. Available: https://www.sirah.com/dyes-accessories/for-high-enery-pulsed-laser/dyes/dcm/. [Accessed 27 January 2021].

[32] Kurt J. Lesker Company, "Kurt J. Lesker Company VPZL-600DU VIEWPORT,Z-L,DUV FUSED SILICA (QUARTZ),6"UHV," Kurt J. Lesker Company, [Online]. Available: https://www.lesker.com/viewports/viewports-cf-flanged-quartz-fused-silica/part/vpzl-600du. [Accessed 27 January 2021].

[33] M. Gragston, *Quick Start Operation Guide for Plasma Microwave Absorption, Scattering, and Xenon Measurement System,* Dayton: Spectral Energies, 2018.

[34] M. N. R. Ashfold, N. H. Nahler, A. J. Orr-Ewing, O. P. J.Vieuxmaire, R. L. Toomes, T. N. Kitsopoulos, I. A. Garcia, D. A. Chestakov, S.-M. Wuc and D. H. Parker, "Imaging the dynamics of gas phase reactions," *Physical Chemistry Chemical Physics,* vol. 8, p. 30, 2006.

[35] J. Yim and J. Burt, "Characterization of Vacuum Facility Background Gas Through Simulation and Considerations for Electric Propulsion Ground Testing," AIAA, Cleveland.

[36] C. Galea, M. Gragston, M. N. Scheider and Z. Zhang, "Coherent Microwave Scattering From Xenon resonance-Enhanced Multiphoton Ionization-Initiated Plasma in Air," *Journal of Applied Physics,* 2020.

[37] M. Goray and R. N. Annavarapu, "Rest Mass of Photon on the Surface of Matter," *Results in Physics,* vol. 16, 2020.

[38] M. Buchanan, "Minkowski, Abraham and the Photon Momentum," Nautre Physics, 2007.

[39] J. T. Kim and J. M. Burt, "Characterization of Vacuum Facility Background Gas Through Simulation and Considerations for Electric Propulsion Ground Testing," NASA, Cleveland, 2015.

[40] G. Danion, M. Vallet, L. Frein, P. Szriftgiser and M. Alouini, "Optoelectric Nibbling of Laser Linewidth Using a Brillouin-Assisted Optical Phase-Locked Loop," Rennes, France, 2018.

[41] Sirah Lasertechnik, "Dyes," Sirah Lasertechnik, [Online]. Available: https://www.sirah.com/dyes-accessories/for-high-enery-pulsed-laser/dyes/. [Accessed 27 January 2021].

[42] Sirah Lasertechnik, *Second Harmonic Generation,* Edinburgh: Photonic Solutions Ltd, 2003.

[43] M. N. R. Ashfold, H. Nahler, A. J. Orr-Ewing, O. P. J. Vieuxmaire, R. L. Toomes, T. N. Kitsopoulos, I. A. Garcia, D. Chestakov, M. Wu and D. H. Parker, "Imaging the Dynamics of Gas Phase Reactions," *Physical Chemistry Chemical Physics* , 2006.

REPORT DOCUMENTATION PAGE

Form Approved
OMB No. 074-0188

1. REPORT DATE *(DD-MM-YYYY)* 25-03-2021	**2. REPORT TYPE** Master's Thesis	**3. DATES COVERED** *(From – To)* December 2019 – March 2021

TITLE AND SUBTITLE

DENSITY MEASUREMENTS OF NEUTRAL XENON USING MULTIPHOTON IONIZATION AND MICROWAVE SPECTROSCOPY IN A HALL EFFECT THRUSTER

5a. CONTRACT NUMBER

5b. GRANT NUMBER

5c. PROGRAM ELEMENT NUMBER

6. AUTHOR(S)

Taylor J. Foy

5d. PROJECT NUMBER

5e. TASK NUMBER

5f. WORK UNIT NUMBER

7. PERFORMING ORGANIZATION NAMES(S) AND ADDRESS(S)

Air Force Institute of Technology
Graduate School of Engineering and Management (AFIT/ENY)
2950 Hobson Way, Building 640
WPAFB OH 45433-8865

8. PERFORMING ORGANIZATION REPORT NUMBER

AFIT-ENY-MS-21-M-329

9. SPONSORING/MONITORING AGENCY NAME(S) AND ADDRESS(ES)

Intentionally left blank

10. SPONSOR/MONITOR'S ACRONYM(S)

11. SPONSOR/MONITOR'S REPORT NUMBER(S)

12. DISTRIBUTION/AVAILABILITY STATEMENT

DISTRUBTION STATEMENT A. APPROVED FOR PUBLIC RELEASE; DISTRIBUTION UNLIMITED.

13. SUPPLEMENTARY NOTES

This material is declared a work of the U.S. Government and is not subject to copyright protection in the United States.

14. ABSTRACT

A new dye laser and microwave scattering system for measuring low speed xenon particles was installed to characterize a commercially sourced 600 W Hall effect thruster. The new system uses multiphoton ionization and microwave spectroscopy to determine number density and velocity measurements of neutral xenon atoms in the plume of a Hall thruster. A study was conducted to ensure the new system will be able to accurately measure these neutrals in future work. The ultimate goal of this new system is to isolate and characterize the extra thrust produced in Hall Effect Thrusters due to finite volume vacuum chambers.

15. SUBJECT TERMS

Hall Thruster, REMPI, Neutral Xenon

16. SECURITY CLASSIFICATION OF:			**17. LIMITATION OF ABSTRACT**	**18. NUMBER OF PAGES**	**19a. NAME OF RESPONSIBLE PERSON** Carl R. Hartsfield, AFIT/ENY
a. REPORT	**b. ABSTRACT**	**c. THIS PAGE**			**19b. TELEPHONE NUMBER** *(Include area code)*
U	U	U	UU	89	(937) 255-3636 x4667 Carl.hartsfield@afit.edu

Standard Form 298 (Rev. 8-98)
Prescribed by ANSI Std. Z39-18